

RESEARCH ARTICLE SUMMARY

HEART DISEASE

Pathogenic variants damage cell composition and single-cell transcription in cardiomyopathies

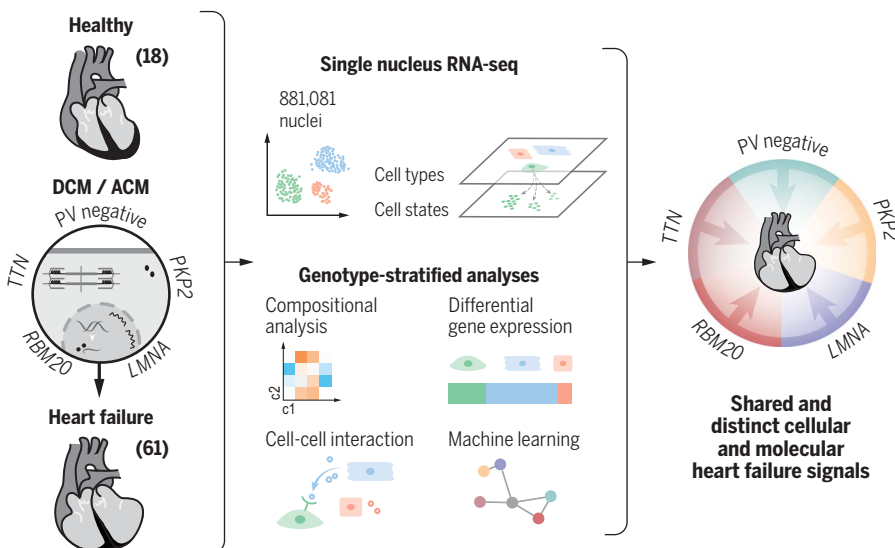
Daniel Reichart†, Eric L. Lindberg*†, Henrike Maatz†, Antonio M. A. Miranda, Anissa Viveiros, Nikolay Shvetsov, Anna Gärtner, Emily R. Nadelmann, Michael Lee, Kazumasa Kanemaru, Jorge Ruiz-Orera, Viktoria Strohmenger, Daniel M. DeLaughter, Giannino Patone, Hao Zhang, Andrew Woehler, Christoph Lippert, Yuri Kim, Eleonora Adami, Joshua M. Gorham, Sam N. Barnett, Kemar Brown, Rachel J. Buchan, Rasheda A. Chowdhury, Chrystalla Constantinou, James Cranley, Leanne E. Felkin, Henrik Fox, Ahla Ghauri, Jan Gummert, Masatoshi Kanda, Ruoyan Li, Lukas Mach, Barbara McDonough, Sara Samari, Farnoush Shahriaran, Clarence Yapp, Caroline Stanasiuk, Pantazis I. Theotokis, Fabian J. Theis, Antoon van den Bogaerd, Hiroko Wakimoto, James S. Ware, Catherine L. Worth, Paul J. R. Barton, Young-Ae Lee, Sarah A. Teichmann, Hendrik Milting†, Michela Noseda†, Gavin Y. Oudit†, Matthias Heinig†, Jonathan G. Seidman*†, Norbert Hubner*†, Christine E. Seidman*†

INTRODUCTION: Human heart failure is a highly morbid condition that affects 23 million individuals worldwide. It emerges in the setting of an array of different cardiovascular disorders, which has propelled the notion that diverse stimuli converge on a common final pathway. Consistent with this, initiating etiologies do not direct heart failure treatments, which are often inadequate and necessitate mechanical interventions and cardiac transplantation.

The recent application of single-nucleus RNA sequencing (snRNAseq) transcriptional analyses to characterize the cellular composition and molecular states in the healthy adult human heart provides an emerging benchmark by which disease-related changes can be assessed.

Moreover, the discovery of human pathogenic variants that cause dilated cardiomyopathy (DCM) and arrhythmogenic cardiomyopathy (ACM), disorders associated with high rates of heart failure, provides direct opportunities to evaluate whether genotype influences heart failure pathways.

RATIONALE: A systematic identification of shared and distinct molecules and pathways involved in heart failure is lacking, and knowledge of these fundamental data could propel the development of more effective treatments. To enable these discoveries, we performed snRNAseq of explanted ventricular tissues from 18 healthy donors and 61 heart failure patients. By focus-



Genotype-stratified analyses of heart failure at the single-nuclei level. The transcriptomes of 881,081 nuclei from 61 heart failure patients were profiled and compared with the transcriptional signatures of 18 healthy controls. Genotype-stratified analyses of cell types and cell state compositions, differential gene expression, cell-cell interactions, and machine learning illuminated the shared and distinct transcriptional signatures resulting from pathogenic variants in DCM and ACM.

ing analyses on multiple samples with pathogenic variants in DCM genes (*LMNA*, *RBM20*, and *TTN*), ACM genes (*PKP2*), or pathogenic variant-negative (PV negative) samples, we characterized genotype-stratified and common heart failure responses.

RESULTS: From 881,081 nuclei isolated from left and right diseased and healthy ventricles, we identified 10 major cell types and 71 distinct transcriptional states. DCM and ACM tissues showed significant depletion of cardiomyocytes and increased endothelial and immune cells. Fibrosis was expanded in disease hearts, but, unexpectedly, fibroblasts were not increased, and instead showed altered transcriptional states that indicated activated remodeling of the extracellular matrix. Genotype-stratified analyses identified multiple transcriptional changes shared only among the hearts harboring pathogenic variants or distinctive for individual and subsets of DCM and ACM genotypes. We validated many of these by single-molecule fluorescent *in situ* hybridization.

Through analyses of receptor and ligand expression across all cells, we observed changes in intercellular signaling and communications, such as increased endothelin signaling in *LMNA* hearts, tumor necrosis factor in *PKP2* hearts, and others. We also identified specific cardiac cell lineages expressing genes with common polymorphisms that were identified in validated association studies of DCM.

Because our findings indicated genotype-enriched transcripts and cell states, we harnessed machine learning to develop a graph attention network for the multinomial classification of genotypes. This network showed remarkably high prediction of the genotypes for each cardiac sample, thereby reinforcing our conclusion that genotypes activate very specific heart failure pathways.

CONCLUSION: snRNAseq of human ventricular samples illuminated cell types and states, molecular signals, and intercellular communications that characterize DCM and ACM. The cellular and molecular architectures that induce heart failure are both shared and distinct across genotypes. These data provide candidate therapeutic targets for future research and interventional opportunities to improve and personalize treatments for cardiomyopathies and heart failure. ■

The list of author affiliations is available in the full article online.
*Corresponding author. Email: eric.lindberg@mdc-berlin.de (E.L.L.); seidman@genetics.med.harvard.edu (J.G.S.); nhuebner@mdc-berlin.de (N.H.); cseidman@genetics.med.harvard.edu (C.E.S.)

†These authors contributed equally to this work.
Cite this article as D. Reichart et al., *Science* **377**, eab01984 (2022). DOI: 10.1126/science.abo1984

S READ THE FULL ARTICLE AT
<https://doi.org/10.1126/science.abo1984>

RESEARCH ARTICLE

HEART DISEASE

Pathogenic variants damage cell composition and single-cell transcription in cardiomyopathies

Daniel Reichart^{1,2,3†}, Eric L. Lindberg^{4,*}, Henrike Maatz^{4,5†}, Antonio M. A. Miranda^{6,7}, Anissa Viveiros^{8,9}, Nikolay Shvetsov⁴, Anna Gärtner¹⁰, Emily R. Nadelmann¹, Michael Lee⁶, Kazumasa Kanemaru¹¹, Jorge Ruiz-Orera⁴, Viktoria Strohmenger^{1,2}, Daniel M. DeLaughter^{1,13}, Giannino Patone⁴, Hao Zhang^{8,9}, Andrew Woehler¹⁴, Christoph Lippert^{15,16}, Yuri Kim^{1,2}, Eleonora Adami⁴, Joshua M. Gorham¹, Sam N. Barnett⁶, Kemar Brown^{1,17}, Rachel J. Buchan^{6,18}, Rasheda A. Chowdhury⁶, Chrystalla Constantinou⁶, James Cranley¹¹, Leanne E. Felkin^{6,18}, Henrik Fox¹⁹, Ahla Ghauri²⁰, Jan Gummert¹⁹, Masatoshi Kanda^{4,21}, Ruoyan Li¹¹, Lukas Mach^{6,18}, Barbara McDonough^{2,13}, Sara Samari⁶, Farnoush Shahriaran²², Clarence Yapp²³, Caroline Stanasiuk¹⁰, Pantazis I. Theotokis^{6,24}, Fabian J. Theis²², Antoon van den Bogaerd²⁵, Hiroko Wakimoto¹, James S. Ware^{6,18,24}, Catherine L. Worth⁴, Paul J. R. Barton^{6,18,24}, Young-Ae Lee^{20,26}, Sarah A. Teichmann^{11,27}, Hendrik Milting^{10†}, Michela Noseda^{6,7†}, Gavin Y. Oudit^{8,9†}, Matthias Heinig^{22,28,29†}, Jonathan G. Seidman^{1†*}, Norbert Hubner^{4,5,30†}, Christine E. Seidman^{1,2,13†}

Pathogenic variants in genes that cause dilated cardiomyopathy (DCM) and arrhythmogenic cardiomyopathy (ACM) convey high risks for the development of heart failure through unknown mechanisms. Using single-nucleus RNA sequencing, we characterized the transcriptome of 880,000 nuclei from 18 control and 61 failing, nonischemic human hearts with pathogenic variants in DCM and ACM genes or idiopathic disease. We performed genotype-stratified analyses of the ventricular cell lineages and transcriptional states. The resultant DCM and ACM ventricular cell atlas demonstrated distinct right and left ventricular responses, highlighting genotype-associated pathways, intercellular interactions, and differential gene expression at single-cell resolution. Together, these data illuminate both shared and distinct cellular and molecular architectures of human heart failure and suggest candidate therapeutic targets.

Dilated cardiomyopathy (DCM), a prevalent disorder occurring in one in 250 individuals, is characterized by left ventricular (LV) dilatation, cardiomyocyte loss with fibrotic replacement, and impaired contractility (1). Arrhythmogenic cardiomyopathy (ACM) similarly incites ventricular dysfunction, often with more prominent right ventricular (RV) involvement, high arrhythmogenic burden, and fibrofatty accumulations (2). Both disorders can arise from genetic causes (1, 2). DCM genes encode proteins involved in contractility [titin (*TTN*),

troponin T (*TNNT2*), troponin C (*TNNC1*), tropomyosin (*TPM1*), and filamin C (*FLNC*) that regulate cardiac splicing [RNA-binding motif protein (*RBM20*)] or calcium sequestration [phospholamban (*PLN*)] and maintain cytoskeletal [desmin (*DES*)] or nuclear [lamin A/C (*LMNA*)] integrity. ACM genes often encode desmosome proteins, including plakophilin-2 (*PKP2*) and desmoplakin (*DSP*). The cardiomyocyte-specific expression and damaging effects of pathogenic variants (PVs) in many DCM and ACM genes propel the development of arrhythmias and heart

failure, a highly morbid condition affecting 23 million individuals worldwide (3).

We hypothesized that PVs in different genes would evoke distinct single-cell molecular phenotypes. To address this, we studied the molecular signals underlying heart failure pathogenesis using single-nucleus RNA sequencing (snRNAseq) of human hearts with advanced DCM and ACM compared with non-failing donor (control) hearts. We revealed differences in the cellular landscape and transcriptional changes between several DCM and ACM genotypes. By leveraging machine-learning approaches, we illuminated genotype-specific molecular responses, as validated by reconstructing the underlying PVs using snRNAseq data.

Results

Study cohort

We studied LV and RV tissues (Fig. 1A) obtained before any mechanical support in 61 patients and 18 controls (tables S1 and S2), including 12 controls previously reported (4). Thirty-eight independent PVs were identified in three DCM genes (*LMNA*, *n* = 12; *RBM20*, *n* = 8; *TTN*, *n* = 12) and in the ACM gene *PKP2* (*n* = 6), whereas no PVs were detected in eight DCM patients (PVneg) (Fig. 1B). Analyses were performed for these five genotypes individually (*n* = 46), for aggregated DCM genotypes (*LMNA*, *RBM20*, *TTN*, and PVneg), ACM (*PKP2*), and controls. Additionally, we generated data from 15 PVs across *PLN*, *BAG3*, *DES*, *FLNC*, *FKTN*, *TNNC1*, *TNNT2*, *TMP1*, and *DSP* (tables S1 and S2). Because there were few recurrent PVs, these genes were excluded in downstream analyses except where indicated.

Males predominated among patients (60%) and controls (72%) (fig. S1A). The mean age of patients was 48.4 ± 4.3 years exclusive of *RBM20* (mean age 32.9 ± 14.6 years). Clinical manifestations indicated similar LV dysfunction in *LMNA*, *TTN*, and PVneg patients, but greater LV dilatation and reduced systolic contraction in *RBM20* and preserved LV with reduced RV function in *PKP2* patients. *LMNA*

¹Department of Genetics, Harvard Medical School, Boston, MA 02115, USA. ²Cardiovascular Division, Brigham and Women's Hospital, Boston, MA 02115, USA. ³Department of Medicine I, University Hospital, LMU Munich, 80336 Munich, Germany. ⁴Cardiovascular and Metabolic Sciences, Max Delbrück Center for Molecular Medicine in the Helmholtz Association (MDC), 13125 Berlin, Germany. ⁵DZHK (German Centre for Cardiovascular Research), Partner Site Berlin, 10785 Berlin, Germany. ⁶National Heart and Lung Institute, Imperial College London, London SW3 6LY, UK. ⁷British Heart Foundation Centre for Research Excellence and Centre for Regenerative Medicine, Imperial College London, London WC2R 2LS, UK. ⁸Division of Cardiology, Department of Medicine, Faculty of Medicine and Dentistry, University of Alberta, Edmonton, Alberta T6G 2R3, Canada. ⁹Mazankowski Alberta Heart Institute, Faculty of Medicine and Dentistry, University of Alberta, Edmonton, Alberta T6G 2R3, Canada. ¹⁰Erich and Hanna Kleemann Institute, Heart and Diabetes Center NRW, University Hospital of the Ruhr-University Bochum, 32545 Bad Oeynhausen, Germany. ¹¹Cellular Genetics Programme, Wellcome Sanger Institute, Wellcome Genome Campus, Hinxton CB10 1SA, UK. ¹²Walter-Brendel-Centre of Experimental Medicine, Ludwig-Maximilian University of Munich, 81377 Munich, Germany. ¹³Howard Hughes Medical Institute, Bethesda MD 20815, USA. ¹⁴Systems Biology Imaging Platform, Berlin Institute for Medical Systems Biology (BIMSB), Max-Delbrück-Center for Molecular Medicine in the Helmholtz Association (MDC), 10115 Berlin, Germany. ¹⁵Digital Health-Machine Learning group, Hasso Plattner Institute for Digital Engineering, University of Potsdam, 14482 Potsdam, Germany. ¹⁶Hasso Plattner Institute for Digital Health, Icahn School of Medicine at Mount Sinai, New York, NY 10029, USA. ¹⁷Cardiac Unit, Massachusetts General Hospital, Boston, MA 02114, USA. ¹⁸Royal Brompton and Harefield Hospitals, Guy's and St. Thomas' NHS Foundation Trust, London SW3 6NR, UK. ¹⁹Heart and Diabetes Center NRW, Clinic for Thoracic and Cardiovascular Surgery, University Hospital of the Ruhr-University, 32545 Bad Oeynhausen, Germany. ²⁰Max Delbrück Center for Molecular Medicine in the Helmholtz Association (MDC), 13125 Berlin, Germany. ²¹Department of Rheumatology and Clinical Immunology, Sapporo Medical University School of Medicine, Sapporo 060-8556, Japan. ²²Computational Health Center, Helmholtz Zentrum München Deutsches Forschungszentrum für Gesundheit und Umwelt (GmbH), 85764 Neuherberg, Germany. ²³Laboratory of Systems Pharmacology, Harvard Medical School, Boston, MA 02115, USA. ²⁴MRC London Institute of Medical Sciences, Imperial College London, London W12 0NN, UK. ²⁵ETB-Bislife Foundation, 2300 AH Leiden, Netherlands. ²⁶Clinic for Pediatric Allergy, Experimental and Clinical Research Center, Charité-Universitätsmedizin Berlin, 13125 Berlin, Germany. ²⁷Department of Physics, Cavendish Laboratory, University of Cambridge, Cambridge CB3 0HE, UK. ²⁸Department of Informatics, Technische Universität Muenchen (TUM), 85748 Munich, Germany. ²⁹DZHK (German Centre for Cardiovascular Research), Munich Heart Association, Partner Site Munich, 10785 Berlin, Germany. ³⁰Charité-Universitätsmedizin Berlin, 10117 Berlin, Germany.

*Corresponding author. Email: eric.lindberg@mdc-berlin.de (E.L.L.); seidman@genetics.med.harvard.edu (J.G.S.); nhuebner@mdc-berlin.de (N.H.); cseidman@genetics.med.harvard.edu (C.E.S.)

†These authors contributed equally to this work.

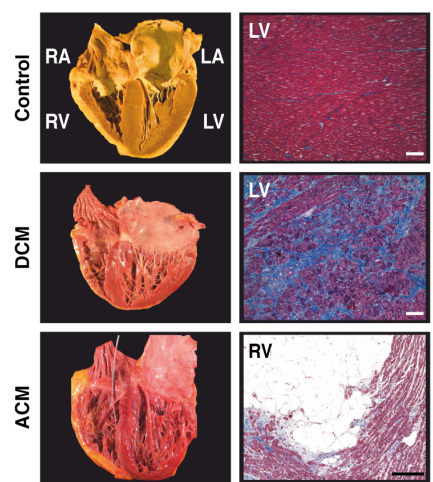
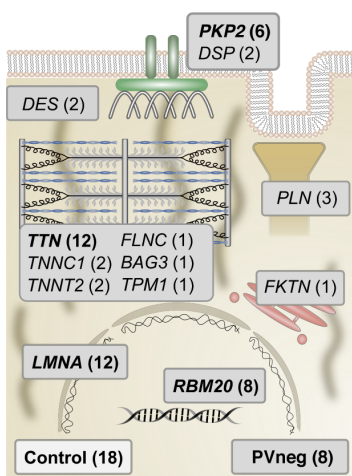
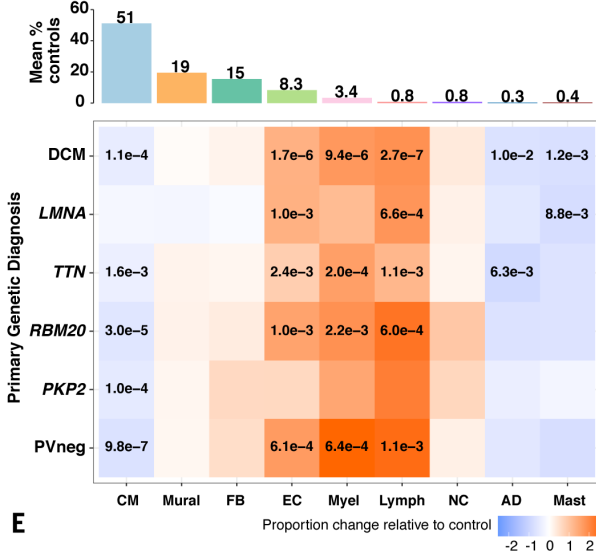
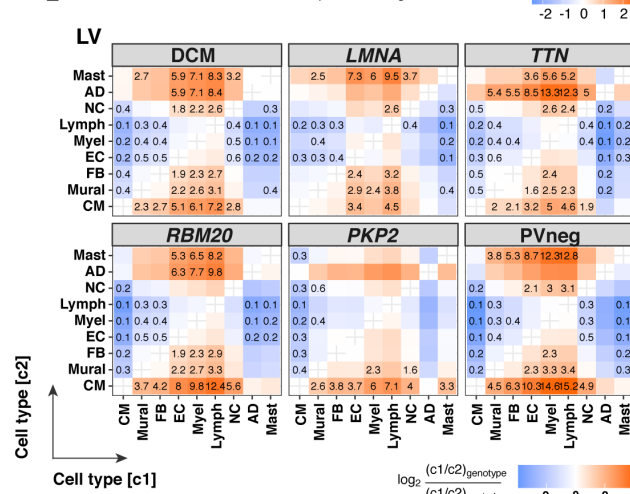
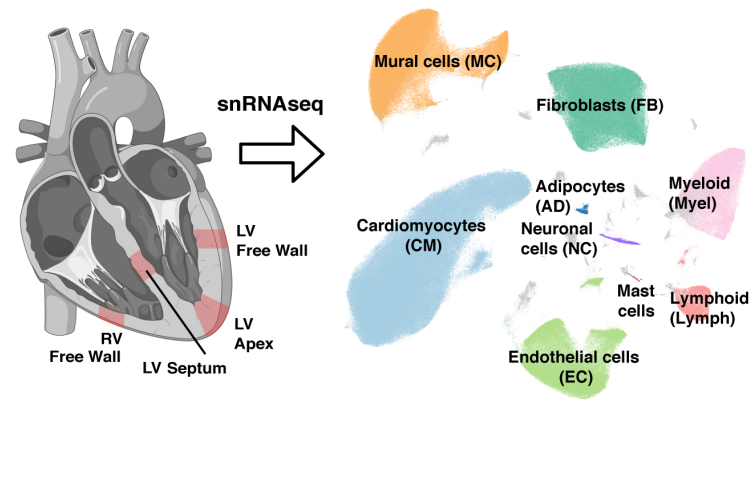
A**B****D****E****C**

Fig. 1. PVs and unexplained causes of DCM and ACM alter cardiac morphology, histopathology, and cellular compositions. (A) Comparisons of normal cardiac anatomy and histology with DCM, demonstrated LV dilation with fibrosis, and ACM-revealed RV dilation with fibrofatty degeneration (Masson trichrome staining; scale bar, 10 μ m). (B) Schematic depiction of the functions of DCM and ACM genes with PVs (number indicates unique genotypes, bold denotes six or more patients) in studied tissues. (C) Single nuclei isolated from transmural LV (free wall, apex, or septum) and RV sections were processed using 10X Chromium 3' chemistry.

UMAP embedding of 881,081 nuclei delineated 10 cell types and unassigned populations (gray). (D) Upper panel: Mean abundance (%) of cell types in control LVs. Lower panel: Proportional changes of cell types in specified genotypes or aggregated across DCM genotypes. Proportional changes are scaled by color: Red indicates an increase and blue a decrease in disease versus control. P values are indicated for significant proportional changes ($FDR \leq 0.05$). (E) Pairwise cell type abundance ratios in specified genotypes or aggregated DCM genotypes in LVs relative to controls. Color scale, FDR, and significance are as in (D).

and *TTN* patients received more pacemaker and/or resynchronization therapies than those with other genotypes (table S1).

Disease-associated compositional changes of cell types

Nuclei were isolated as described previously (4) from full thickness LV free wall, apex, septum, and RV free wall (Fig. 1C). We compared ~500,000 high-quality nuclei from patients' ventricular tissues and ~380,000 nuclei from controls (fig. S1, B to E). After preprocessing and quality control filtering, data were integrated across samples using Harmony before

constructing manifolds using Uniform Manifold Approximation and Projections (UMAPs). Clustering identified 10 major cardiac cell types encompassing ventricular cardiomyocytes (CMs), fibroblasts (FBs), adipocytes (ADs), pericytes and smooth muscle cells (mural, MCs), endothelial cells (ECs), myeloid and lymphoid (immune cells), neuronal (NCs), and mast cells (Fig. 1C) with 71 distinct cell states. States of the same cell type shared a transcriptional profile but also expressed distinct genes, which implied biological differences.

Cell type abundances in sample replicates were highly correlated (Pearson coefficient

0.74 to 0.99) (fig. S2, A and B). Cell composition, states, and transcript counts across the free wall, apex, and septum showed high similarities, and therefore are reported grouped together as LV (fig. S2, C and D).

Using center log ratio-transformed abundance of cell types, we considered the effects of sex on LV and RV cell compositions in DCM ($n = 10$ female, $n = 29$ male) and control ($n = 7$ female, $n = 11$ male) hearts (fig. S2E). Myeloid cells showed a modest sex-specific difference [false discovery rate (FDR) = 0.016]. Only *LMNA* tissues (from $n = 7$ males and $n = 5$ females) were sufficient for genotype-specific, sex-associated

analyses. Female LV myeloid cells were increased ($FDR = 0.05$), paralleling the findings in DCM versus controls. In addition, RV endothelial cells showed a modest female-specific increase between *LMNA* patients and controls ($FDR = 0.048$).

The proportions of LV nuclei across the genotypes demonstrated depletion of CMs except in *LMNA*, and increased ECs and immune cells except in *PKP2* (Fig. 1D and fig. S3). In RVs (fig. S4), CMs were depleted in the DCM subgroup except for *TTN*, whereas ECs were increased in *LMNA*, *TTN*, and *RBM20*, and immune cells were not changed. FBs were not increased in LVs and RVs (Fig. 1D) despite histopathological findings of fibrosis, which implied the acquisition of a secretory rather than a proliferative phenotype.

Individual-level abundances for cell types (LV, table S3; RV, table S4) and cell states (table S5) are provided for controls and patients. Different cell type abundances in disease compared with control LVs remained significant using a linear model adjusting for age. Pairwise cell type ratios in disease LVs compared with controls confirmed loss of CMs and showed accompanying increased ECs, lymphoid and myeloid cells, and altered ratios (FB and mural cells compared with CMs) with quantitative, genotype-specific differences (Fig. 1E). *RBM20* and PVneg, respectively, showed greatest shifts in the EC:CM (8- and 10.3-fold), myeloid:CM (9.8- and 14.6-fold), and lymphoid:CM (12.4- and 15.2-fold) ratios. By contrast, pairwise ratios of all cell types compared with CMs were modest or unchanged in *LMNA*.

Genotypes diversify cell types and states

Cardiomyocytes

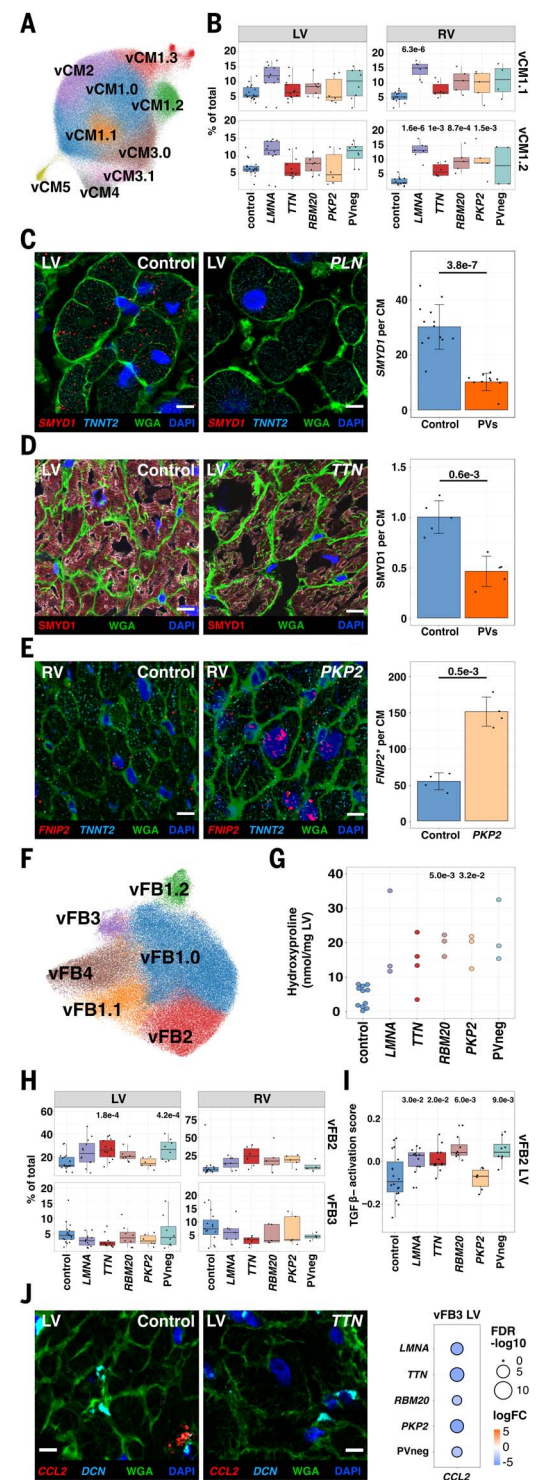
Disease and control ventricles exhibited the previously described cardiomyocyte states, vCM1.0 to vCM5 (4), and four new states, vCM1.1, vCM1.2, vCM1.3, and vCM3.1 (Fig. 2, A and B, and table S6). Across all vCM cell states (fig. S5), differentially expressed genes (DEGs) in disease connoted increased stress (e.g., *NPPB*) and apoptosis (tables S7 to S12 and fig. S6A). Although these findings implied late-stage transcriptional convergence, 20 to 40% of DEGs were genotype specific (fig. S5). Only PVneg reduced *MYH6* expression, increasing *MYH7:MYH6* ratios (fig. S6B). Conversely, only vCMs with PVs down-regulated *SMYD1* (Fig. 2C; fig. S6, C to E; table S13), a cardioprotective muscle-specific histone methyltransferase that regulates sarcomere assembly and mitochondrial energetics (5, 6), and *ADRB1* (β -adrenergic receptor; fig. S6C), which is indicative of adrenergic activation and is therapeutically targeted by β -blockade medicines (7, 8). Genotype-selective responses included up-regulation of *FNIP2* (Fig. 2D), inhibiting AMP-activated protein kinase activity

Fig. 2. Cardiomyocytes and fibroblast states in control, DCM, and ACM ventricles.

(A) UMAP depicting CM states in all tissues. (B) Control and disease LV and RV abundance analyses for vCM1.1 (upper panel) and vCM1.2 (lower panel). (C) Single-molecule RNA fluorescent in situ hybridization exemplifies decreased *SMYD1* (red) expression in CMs (identified by *TNNT2* transcripts, cyan) within a DCM heart with a PV in *PLN* (phospholamban). Cell boundaries are stained with WGA (green); nuclei are stained with DAPI (blue). Scale bar, 10 μ m. Quantified expression (spots per CM) and *P* values from four independent control and disease LVs with PVs were assessed. (D) Immunohistochemistry validated decreased *SMYD1* (red) protein in CMs (identified by troponin T staining, fig. S6E) in TTN LV section. Cell boundaries are stained with wheat germ agglutinin (WGA; green); nuclei are stained with 4',6-diamidino-2-phenylindole (DAPI; blue). Scale bar, 10 μ m. Quantified protein levels (intensity per CM) and *P* values were assessed from five independent control and DCM LVs with PVs. (E) Single-molecule RNA fluorescent in situ hybridization demonstrated increased expression of *FNIP2* (red). CMs, nuclei, and cell boundaries are labeled as in (C). Scale bar, 10 μ m. Quantified expression of *FNIP2* (spots per CM and H-score) and *P* values reflect analyses of two independent control and *PKP2* samples. (F) UMAP depicting FB states. (G) Hydroxyproline assay (HPA) quantified cardiac collagen content for each genotype. (H) Control and diseased LV and RV abundance analyses for vFB2 (upper panel) and vFB3 (lower panel). (I) Pathway score of *TGF β* activation in LV vFB2. (J) Single-molecule RNA fluorescent in situ hybridization showing decreased expression of *CCL2* (red) in vFB3 (DCN, cyan) in disease compared with controls. Cell boundaries are stained with WGA (green); nuclei are stained with DAPI (blue). Scale bar, 10 μ m. Dot plot illustrating the log 2 fold change (log 2 FC) and significance [$-\log_{10}(FDR)$] of *CCL2* expression in LV vFB3 across genotypes.

and oxidative metabolism (9–11) in *LMNA* and *PKP2*, and *CPEB4*, an RNA-binding protein that activates glycolysis and stimulates fibrosis (12) in *LMNA*, *RBM20*, and *PKP2* (fig. S6F).

Proportional differences in vCM states (figs. S6G, S7, and S8) varied among genotypes and controls and were more prominent in RVs than LVs, perhaps reflecting hemodynamic differences. PVs generally increased vCM1.1



and vCM1.2, with accompanying decreased vCM3.1 in *LMNA* and *TTN* (Fig. 2B and figs. S7A and S8, A to D). State-enriched DEGs for vCM1.1 included *MYO18B*, which is required for sarcomere formation (13); *XPR1*, which regulates phosphate homeostasis (14); and *IGF1R* and *ROR1*, which are involved in cell survival (8). vCM1.2 had heightened expression of electrophysiologic genes including

PCDH7, which enables intercellular contacts (15, 16) but when overexpressed impedes synaptic currents (17); *CAMK2D*, which modulates excitation-contraction coupling (18); and *ANK2*, which harbors arrhythmogenic PVs (19, 20). vCM1.3 was modestly increased in *RBM20*, associated with the largest numbers of DEGs in all genotypes, and enriched for *BMP* receptors [*BMPRIA1*, *BMPR1B* (21, 22); fig. S7, B and D] and *GPC5*, which regulates *BMP* signaling (23). vCM3.1, which was reduced in *LMNA* and *TTN*, expressed early-adaptive transcriptional regulators of stress responses (*ATF3* and *ATF4*) and cardioprotection (*NR4A3*; fig. S7E) (24). Only PVneg depleted vCM2 and was enriched for *SH3RF2*, an anti-apoptosis regulator of the *JNK* pathway (25). Because DCM and ACM genes are highly and often selectively expressed in CMs, these disease-associated vCM states and DEGs defined intrinsic responses to PVs as well as cell-cell responses to CM death, and depressed contractile performance and arrhythmogenicity.

Fibroblasts

We identified four previously characterized FB states (4) and two new ones, vFB1.1 and vFB1.2 (Fig. 2E and table S14). Across all vFB states, up-regulated DEGs included genes involved in extracellular matrix (ECM) remodeling (figs. S9 to S11 and tables S15 to S21). *LMNA*, *TTN*, and *PKP2* increased fibrogenic signaling receptor, and *EGFR* and *PKP2* also increased *AGTR1* (fig. S10A), which enables EGFR transactivation (26, 27). The expression of profibrotic *TGFβ2* was universally increased (fig. S10B). DCM hearts were enriched for *PCOLCE2*, promoting insoluble collagen formation (28), and *LMNA*, *TTN*, and PVneg down-regulated metalloproteinase inhibitors *TIMP1* and *TIMP3* (fig. S10C). Collagen genes showed genotype-specific expression. *COL4A1* and *COL4A2* were up-regulated in *LMNA*, *TTN*, and *PKP2*, whereas *COL4A5* and *COL24A1* were enriched in PVneg. Thus, although ECM up-regulation and collagen deposition (Fig. 2F and fig. S10, D to F) were shared features, genotype and chamber influenced composition and organization.

FB state abundance was also altered across genotypes (figs. S11A and S12, A to D). vFB1.1 and vFB1.2 expressed canonical vFB1.0 genes, but vFB1.1 also up-regulated *APOD*, *APOE*, and *APOO*, which typify lipogenic fibroblasts (29), and *CST3* (fig. S13A), which is involved in matrix remodeling. vFB1.2-enriched genes are related to actin filament assembly (*DAAM1*) and chondrocyte differentiation (*GPC6*) (fig. S13B). vFB2 expressed prominent profibrotic genes, including *TGFβ* targets (increased in DCM LVs) and fibrogenic *IL11* (30) (highest in *RBM20* LVs) (Fig. 2H and fig. S14, A to C). vFB2 was increased in *TTN* and PVneg and modestly in other DCM LVs (Fig. 2, G and H, and fig. S11).

vFB3, which was diminished in hearts with PVs, expressed proinflammatory cytokine genes (*CCL2*) and genes related to *OSM* signaling (*JL6ST*, *OSMR*, and oncostatin M-target genes) (Fig. 2I and fig. S14D). The resultant increased ratio of vFB2:vFB3 and altered DEGs suggested dysregulation of fibroblast-to-macrophage interactions that would promote deleterious ECM remodeling, particularly in *TTN* LV and RV (fig. S12, C and D).

Smooth muscle cells and pericytes

Three previously described pericyte cell states (PC1, PC2, and PC3) and three smooth muscle cell states (SMC1.1, SMC1.2, and SMC2; Fig. 3A and table S22) were identified. DEGs across all states (fig. S15 and tables S23 to S28) showed up-regulation of the sodium channel *SCN3A*, with unknown vascular functions, and the noncoding antisense *ADAMTS9-AS2*, with concordant down-regulation of *ADAMTS9*, a metalloprotease involved in ECM remodeling (31, 32) (Fig. 3B and fig. S16A). Overall, the genes with dysregulated expression indicated that disease evoked signals to synthesize specific ECM and integrin components.

DEGs in PC states included down-regulation of two central signaling receptors, *NOTCH3* and *PDGFRB*, in *PKP2* and *TTN* PC1 (Fig. 3B). *NOTCH3* is required for SMC maturation and deficiency causes pericyte dysfunction and arteriovenous malformations. Notch signaling regulates *PDGFRB*, which is necessary for angiogenesis and PC recruitment (33–37).

DEGs in SMCs subdivided the previously identified canonical SMC1 (4) into two states: SMC1.1, which had higher expression of *ACTA2*, *MYH11*, and *TAGLN*, and SMC1.2, which strongly expressed *ITGA8*, required for maintenance of SMC contractile phenotype (38, 39), and *ATP10A*, suggesting vascular stiffness and increasing diastolic dysfunction (Fig. 3B). Methylation of the *ATP10A* locus in SMC decreases with age and atherosclerosis (40). SMC1.2 was enriched in *LMNA*, *TTN*, and PVneg RVs (figs. S17 and S18). SMC2 expressed high levels of genes involved in collagen and elastic fiber formation (*ELN* and *LAMA2*) and *MYH10*, demarcating dedifferentiated SMCs with secretory properties (figs. S16B and S17C). *LMNA* and *PKP2* SMC2 up-regulated *SLIT3*, a stimulator of fibroblast activity (41), and ECM synthesis and collagen formation genes (Fig. 3, B and C). Collectively, disease remodeling of MC indicated modulation of PDGF and NOTCH signaling receptors and synthesis of selective ECM and integrin components.

Endothelial cells

Characterization of ECs identified seven previously described cell states (4): EC1, EC2, EC5 to EC8 and mesothelial cells (Fig. 3D, figs. S19 to S21, and table S29). Shared DEGs occurred across all and between genotypes

(tables S30 to S35), with clear RV and LV differences (fig. S19). Dysregulation of genes encoding factors involved in EC fate, blood vessel development, and angiogenesis (*NOTCH4*, *FLT1*, *FGFR1*, and *RGCC*) (42–44) in disease LVs indicated that vascular remodeling was a common heart failure feature.

EC composition in DCM RVs and LVs increased EC5 compared with controls (fig. S21A), whereas genotype-specific cell state ratios in LVs generally decreased EC1 relative to EC2, EC5, and EC6 (Fig. 3F and fig. S21C). Assessment of selective gene enrichment scores for proliferating cells, endothelial-to-mesenchymal transformation, and cell death showed no difference in disease compared with controls (fig. S22 and table S36).

EC7 had the most DEGs and the highest proportion of unique DEGs across all genotypes. Although initially defined as being atrial-enriched (4), EC7 expressed endocardial-enriched genes [*SMOC1* (45), *NPR3* (46), and *POSTN* (47)] (fig. S20, B and C), which prompted a revised annotation to endocardial cells. Up-regulated genes in EC7 from DCM LVs and *PKP2* RVs (Fig. 3G) encoded secreted proteins involved in myocardial stress adaptation (*NRG1*) (48), CM force production (*EDNI*) (49, 50), and endocardial expansion during development or after cardiac injury (*BMP6*) (51, 52). *BMP6* was selectively up-regulated in the endocardium of DCM LVs and ACM RVs (Fig. 3E). Conversely, *INHBA*, a TGF- β superfamily member involved in atrioventricular canal development (53), and cell adhesion molecule *OPCML* were down-regulated. In *PKP2*, an unconventional myosin promoting cell adhesion (*MYO10*), and *POSTN* were up-regulated in both ventricles. These data highlighted the involvement of the endocardium in chamber-specific remodeling of cardiomyopathies.

Myeloid cells

We classified 14 subclusters of myeloid cells comprising macrophages (MPs), monocytes (MOs), conventional dendritic cells (cDC1 and cDC2), and proliferating myeloid cells (Fig. 4A, figs. S23 to S27, and tables S37 to S45). Distinct gene sets were unique to each genotype and were particularly pronounced in PVneg and *PKP2* in LVs (fig. S24).

Although disease increased myeloid cells, the proportions of proliferating myeloids (Fig. 4, B and C, and figs. S26 and S27) were consistently lower compared with controls, implying monocyte infiltration. The tissue-resident MPs *LYVE1*^{high}*MHCII*^{low} and *LYVE1*^{low}*MHCII*^{high} (fig. S25C) were the most abundant myeloid cells (fig. S27, A and B). MP *LYVE1*^{low}*MHCII*^{high} were increased in the RV of *LMNA*, with similar trends in other genotypes (fig. S27B). Proportions of MP^{OSM} were modestly decreased with down-regulation of *OSM* in *TTN* ventricles (fig. S28A), which would attenuate the

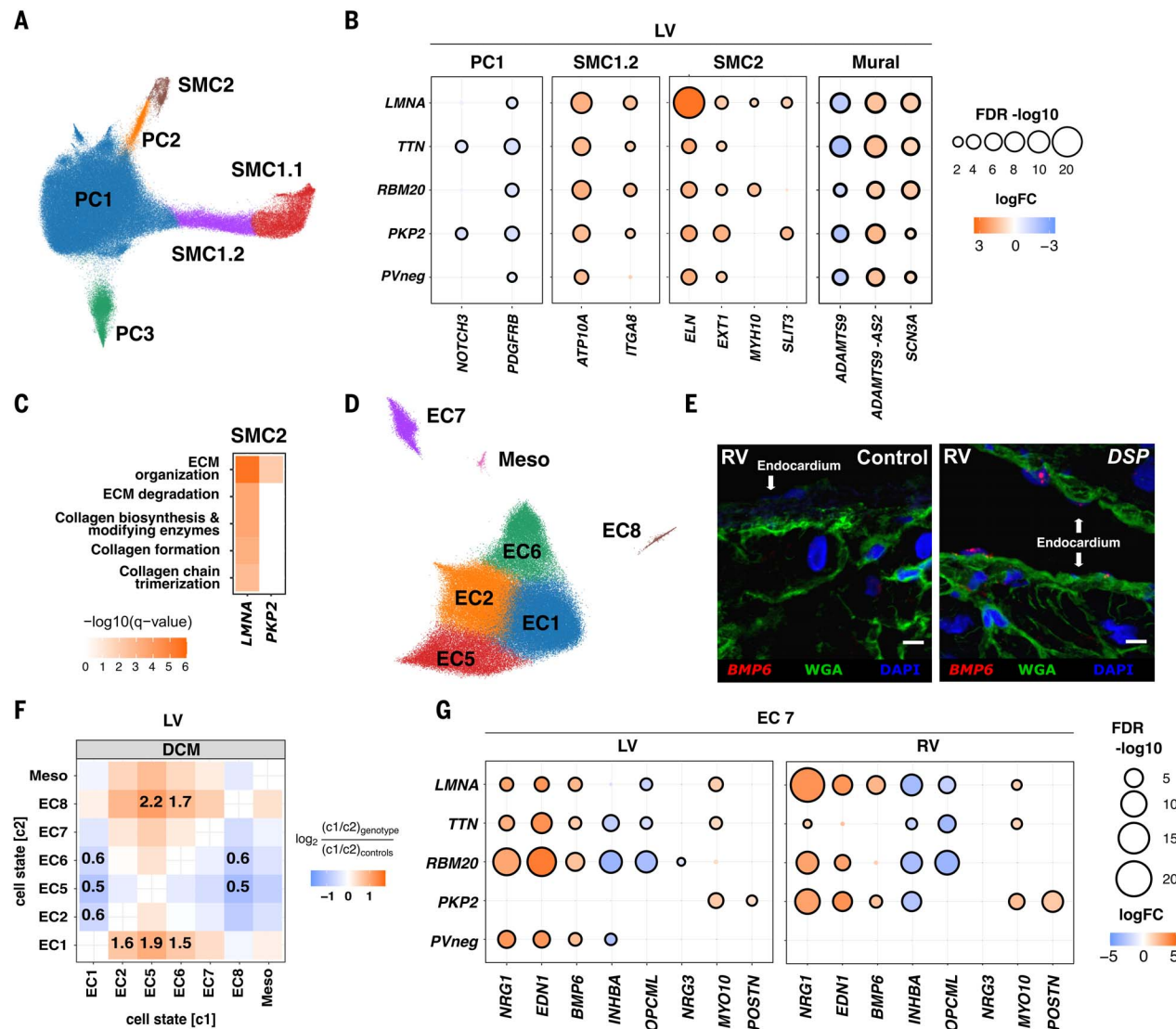


Fig. 3. Mural and endothelial cell states in control, DCM, and ACM hearts.
(A) UMAP depicting PC and SMC states in all tissues. **(B)** Dot plots illustrating the levels (fold-change; logFC) and significance [$-\log_{10}(\text{FDR})$] of selected DEGs in LV PC1, SMC1.2, SMC2, and MC (PC and SMC) across genotypes. **(C)** KEGG pathway analysis of DEGs in SMC2 among genotypes with one or more enriched pathways. Color intensity denotes enrichment significance [$-\log_{10}(\text{FDR})$]. **(D)** UMAP depicting EC states in all tissues. **(E)** Single-molecule RNA fluorescent in situ hybridization identified *BMP6* (red) expression in the RV endocardium

from a heart with a DSP (desmoplakin) PV compared with control RV. Cell boundaries are stained with WGA (green); nuclei are stained with DAPI (blue). Scale bar, 10 μm . **(F)** Pairwise cell state abundance ratios in DCM LVs relative to controls. Proportional changes are scaled by color: Red indicates an increase and blue a decrease in disease versus control. P values are indicated for significant proportional changes ($\text{FDR} < 0.05$). **(G)** Dot plots illustrating LV and RV levels (fold-change; logFC) and significance [$-\log_{10}(\text{FDR})$] of selected DEGs in EC7 across genotypes. Dot size and color are as defined in (B).

MP^{OSM}-vFB3 signaling axis (4), and mirrored the decreased OSM pathway activation score observed in vFB3 (fig. S14B).

Prominent antigen-presenting activities were evident in MO^{VCAN}, MO^{CD16}, cDC1, and cDC2, and also occurred in MP^{FOLR2}, akin to tumor-associated MPs (54). Across antigen-presenting MPs, *RBM20* LVs showed the highest presentation of antigens based on MHCII genes (fig. S28, B and C) and more abundant cDC2 compared with the other genotypes (fig. S27). *PKP2* LVs up-regulated MP^{ISG} (fig. S27) with interferon-stimulated genes (55), perhaps

contributing to inflammatory *PKP2* phenotypes (56).

Lymphoids

We classified 15 lymphoid cell states, including T and natural killer (NK) cell subsets, innate lymphoid cells (ILCs), B cells, plasma cells, and proliferating lymphoids (Fig. 4D, figs. S29 to S32, and table S46). Our experimental design did not enrich for immune cells, and few (<40) genotype-specific DEGs were identified (fig. S29). Proliferating lymphoids were rare, and their abundance was

unchanged in disease (figs. S30 and 32, A to D, and tables S47 to S52).

The cardiac complexity of CD4⁺ and CD8⁺ T cells included naive (CD4T^{naive}), activated (CD4T^{act}), regulatory (CD4T^{reg}), cytotoxic (CD8T^{cytotoxic}), transitional (CD8T^{trans}), terminal effector (CD8T^{te}), and effector memory (CD8T^{em}) cells (fig. S31B) (57). We detected increased CD4T^{act} only within DCM samples (fig. S32, A to D). However, DEGs indicated lymphocyte activation (cytokines *IFNG*, *CCL3*, and *CCL4* and signaling molecules *CBLB*, *FYN*, and *TXNIP*), and maturation (cell surface

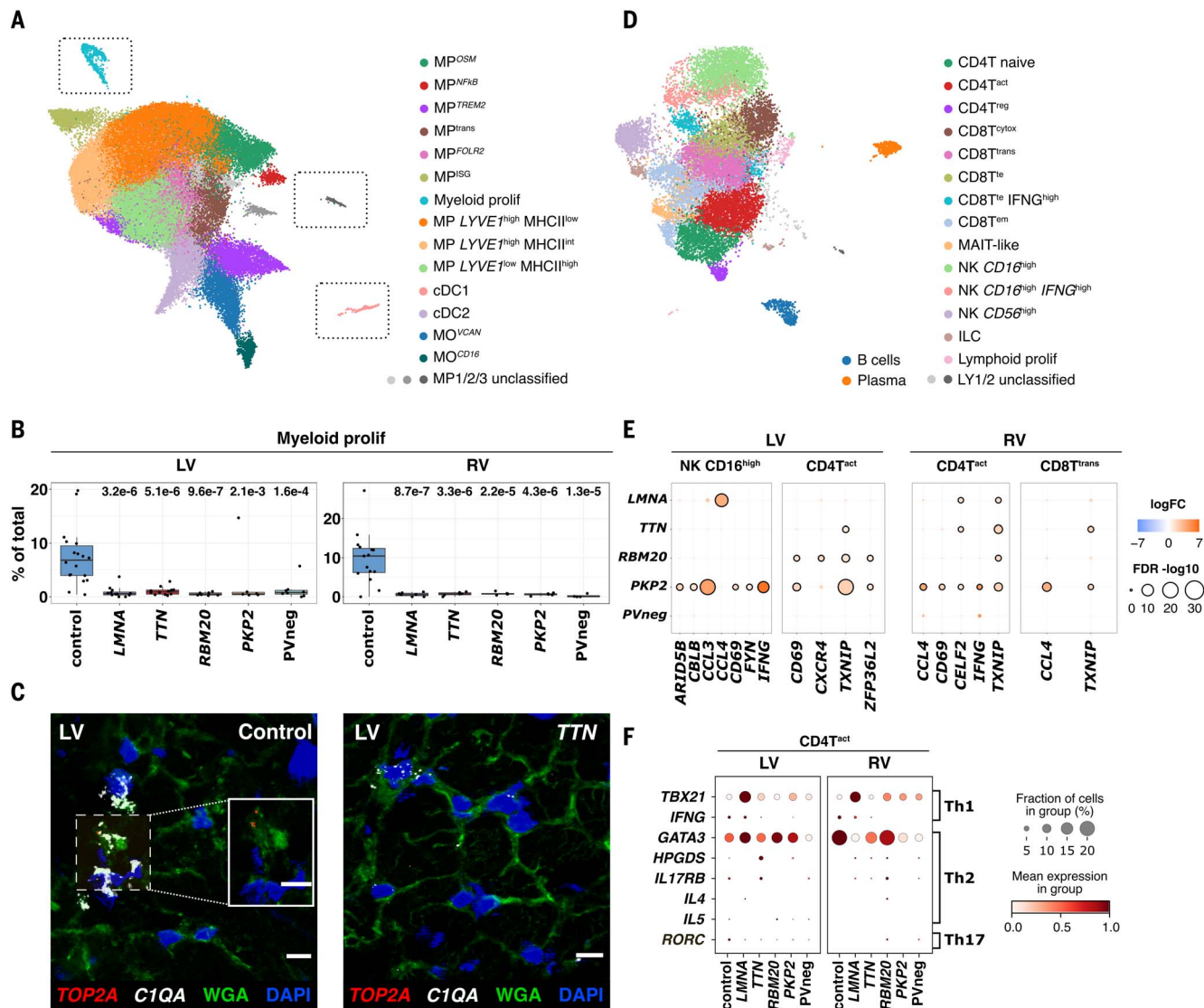


Fig. 4. Immune cell states in control, DCM, and ACM hearts. (A) UMAP depicting myeloid states in all tissues. Unclassified MP1, MP2, and MP3 require future characterization. Gray boxes enclosing proliferating (prolif) MPs, unclassified MPs, and cDC1s indicate that these were manually moved toward other states for ease of representation. The unmodified UMAP is in fig. S23. (B) Myeloid proliferation had higher abundance (% total myeloids) in controls versus disease. P values indicate significant differences in abundances. (C) Single-molecule RNA fluorescent in situ hybridization validated increased expression of TOP2A (red) and

C1QA (white) in controls versus disease. Cell boundaries are stained with WGA (green); nuclei are stained with DAPI (blue). Scale bar, 10 μ m. (D) UMAP depicting lymphoid cell states in all tissues. Unclassified LY1 and LY2 require future characterization. (E) Dot plots showing the level of fold-change (logFC) and significance [$-\log_{10}(\text{FDR})$] of selected genes in LV NK CD16^{hi}, LV and RV CD4T^{act}, and RV CD8T^{trans} across genotypes. (F) Dot plots highlighting gene expression of the Th1, Th2, and Th17 signatures in CD4T^{act} cells. Dot size indicates the fraction (%) of expressing cells; color indicates the mean expression.

receptors CD69 and CXCR4), particularly in PKP2 NK⁻ cells, CD4⁺ T cells, and CD8⁺ T cells (Fig. 4E).

CD4⁺ helper T cells are critical drivers in the pathogenesis of cardiomyopathy and myocarditis (58, 59). In LMNA CD4T^{act} cells, we observed up-regulation of TBX21, which is important for Th1 polarization. Conversely, the Th2-polarization transcription factor GATA3 was down-regulated in PVneg (Fig. 4F).

Neuronal cells

Analysis of cardiac NCs was limited by rarity of this cell type (Fig. 5A, fig. S33, and tables S55

to S57). Across all NC states, DEGs indicated increased NFATC2 in LVs with PVs and PKP2 RVs, and genotype-selective enrichment of LRRK2, an activator of a neurotoxic cascade (60). Other up-regulated DEGs function in proteoglycan synthesis for neuronal myelination and axon regeneration (XYLT1 and HS3ST4), and a complement inhibitor (SUSD4) that affects neural function and morphology (61, 62). Genotype-specific DEGs were highest in PKP2.

We identified previously described NC states (4) and three new ones (Fig. 5, B and C, and figs. S34 and S35) that were genotype and

chamber selective: NC1.1 in LMNA and TTN LVs; NC1.2 in TTN and RBM20 LVs and in LMNA, TTN, and PKP2 RVs. NC1.1 was distinguished by the highest up-regulation of NFATC2. NC1.2 up-regulated genes associated with electrocardiogram intervals (SLC35F1 and AJAPI; Fig. 5D), IGFBP5, involved in neuronal apoptosis and autophagy, and the ion channel and heart rate regulator KCNK1 (63–65). NC1.3 was enriched for the neuromodulator receptor GALR1 and phosphodiesterases PDE10A and PDE3B, which participate in neuroprotection and signaling (66–68). Dysregulated expression of genes involved in stress responses and

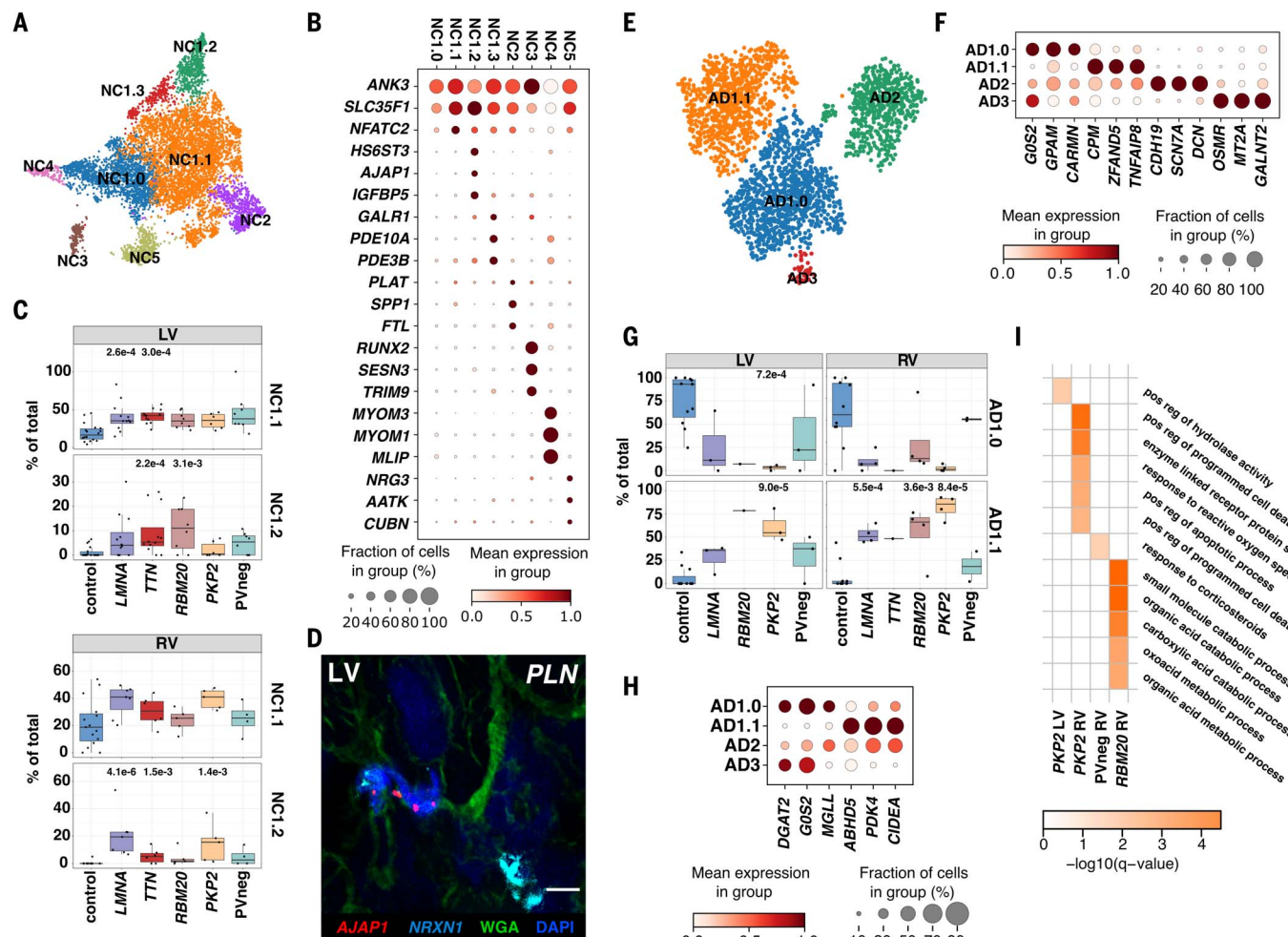


Fig. 5. Neuronal and adipocyte cell states in control, DCM, and ACM hearts. (A) UMAP depicting NC states in all tissues. (B) Dot plot highlighting the top marker genes for NC states. (C) LV and RV abundance analyses of NC1.1 and NC1.2 in controls versus disease. *P* values are indicated for significant proportional changes (FDR ≤ 0.05). (D) Single-molecule RNA fluorescent in situ hybridization showing colocalization of AJAP1 (red) and NRXN1 (cyan) in disease as exemplified in a DCM LV with a PV in PLN (phospholamban) demarcating the NC1.2 state. Cell boundaries are stained with WGA (green); nuclei are stained with DAPI (blue).

electrophysiology may account for characteristic life-threatening arrhythmias in DCM and PVs in *PKP2* (1, 2).

Adipocytes

Similar to NCs, limited adipocytes were captured. We identified three adipocyte states previously found in controls: canonical AD1.0, expressing lipid metabolism genes; stromal AD2, expressing ECM genes; and immune AD3, expressing *OSMR* and cytokine-responsive genes (Fig. 5, E and F, fig. S36, and tables S60 to S64). Although AD3 was not detected in disease, a fourth identified state, AD1.1, was almost exclusive to diseased hearts (Fig. 5G and fig. S37). Compositional analysis identified increased proportions of AD1.1 in *PKP2* LVs and RVs concurrent with decreased LV

proportions of AD1.0. *LMNA* and *RBM20* RVs, unlike LVs, also increased proportions of AD1.1 (fig. S38, A to D).

DEGs between AD1.1 and AD1.0 revealed changes in fatty acid metabolism pathways (Fig. 5H). AD1.1 showed down-regulation of *DGAT2*, encoding a triglyceride-forming enzyme (69), and *GOS2* and *MGLL*, encoding lipolysis regulators (70). Conversely *ABHD5*, a positive lipolysis regulator (70, 71); *PDK4*, a kinase promoting the shift from glucose to fatty acid metabolism; and *CIDEA*, a regulator of adipose tissue energy expenditure, were up-regulated. *PKP2* RVs, which typically display fibrofatty replacement, also showed an enrichment of Gene Ontology biological processes for apoptosis and cell death (Fig. 5I). These data implied genotype-specific state transitions or

replacement of canonical adipocytes in DCM and ACM.

Differential expression of GWAS genes in cardiomyopathies

Genome-wide association studies (GWAS) have identified common genetic variants associated with DCM. We selected candidate genes from 15 previously identified DCM loci (table S67) and examined expression across cell types and genotypes (fig. S39). Overall, GWAS genes were more often DEGs in LV and RV than expected by chance in snRNAseq data [LV: odds ratio (OR) = 7.0, *P* = 0.0007; RV: OR = 6.1, *P* = 0.0009, one-sided Fisher's exact test]. Multiple genes showed cell-type-specific expressions, with the majority highly enriched in CM (*ALPK3*, *BAG3*, *FHOD3*, *FLNC*, *HSPB7*, *MLIP*, *SLC6A6*,

SMARCB1, *SVIL*, and *TTN*). Among these, we observed both genotype- and chamber-specific expression differences. The heat shock protein *HSPB7* was reduced in *TTN* LVs and in *LMNA* and *PKP2* RVs. *SLC6A6*, a taurine and amino acid transporter with cardioprotective effects, was increased in both LV and RV across all genotypes except for *PKP2* and *PVneg*. *CDKN1A*, a cell cycle regulator and modulator of apoptosis (72), was increased in *LMNA* CMs from LVs but not RVs (72).

GWAS genes that were more broadly expressed across cell types included *MTSS1*, encoding a putative actin-cytoskeletal interactor. *MTSS1* showed highest and unchanged expression in myeloids and was widely increased in mural cells as well as in FBs in *LMNA*, *TTN*, and *PKP2* (fig. S39), suggesting influences beyond direct effects on CM function (73, 74).

SLC39A8, a lowly expressed cardiac solute carrier, was unchanged in CMs but increased in *LMNA* and *TTN* LV ECs. We suggest that cell-specific expression changes of GWAS genes may improve interpretation of their biologic effects.

Predicted and altered cell-cell interactions across genotypes

By examining the expression of genes encoding for receptors and ligands, we inferred intercellular signaling and communication (75). We initially quantified the probability of cell-cell interactions and compared signaling between cell states, and then aggregated information to produce cell-specific and across-all-cell-types data for each genotype relative to controls. This sequential approach accounted for differential abundances of cell states.

We detected aberrant intercellular signaling across disease (Fig. 6A and fig. S40), including up-regulation of the BMP, FN1, collagen, EGF, IGF, and TGF pathways that promote fibrosis. Signaling dependent on VEGF, NOTCH, and ANGPT was also increased in disease, implying vascular remodeling. Genotype-selective increases in intercellular signaling pathways were also identified in LVs (Fig. 6B and fig. S40, A and B): EDN in *LMNA*, the proinflammatory IL6 in *TTN*, BAFF/LIGHT (denoting TNF signaling) in *RBM20*, pro-inflammatory CCL and TNF in *PKP2*, and the immune modulator BTLA in *PVneg*. Some of these intercellular signaling pathways were similarly dysregulated in RV, but chamber-specific changes were also observed (fig. S40, C and D, and fig. S41).

We also identified genotype-specific differences in the cells sending and receiving signals

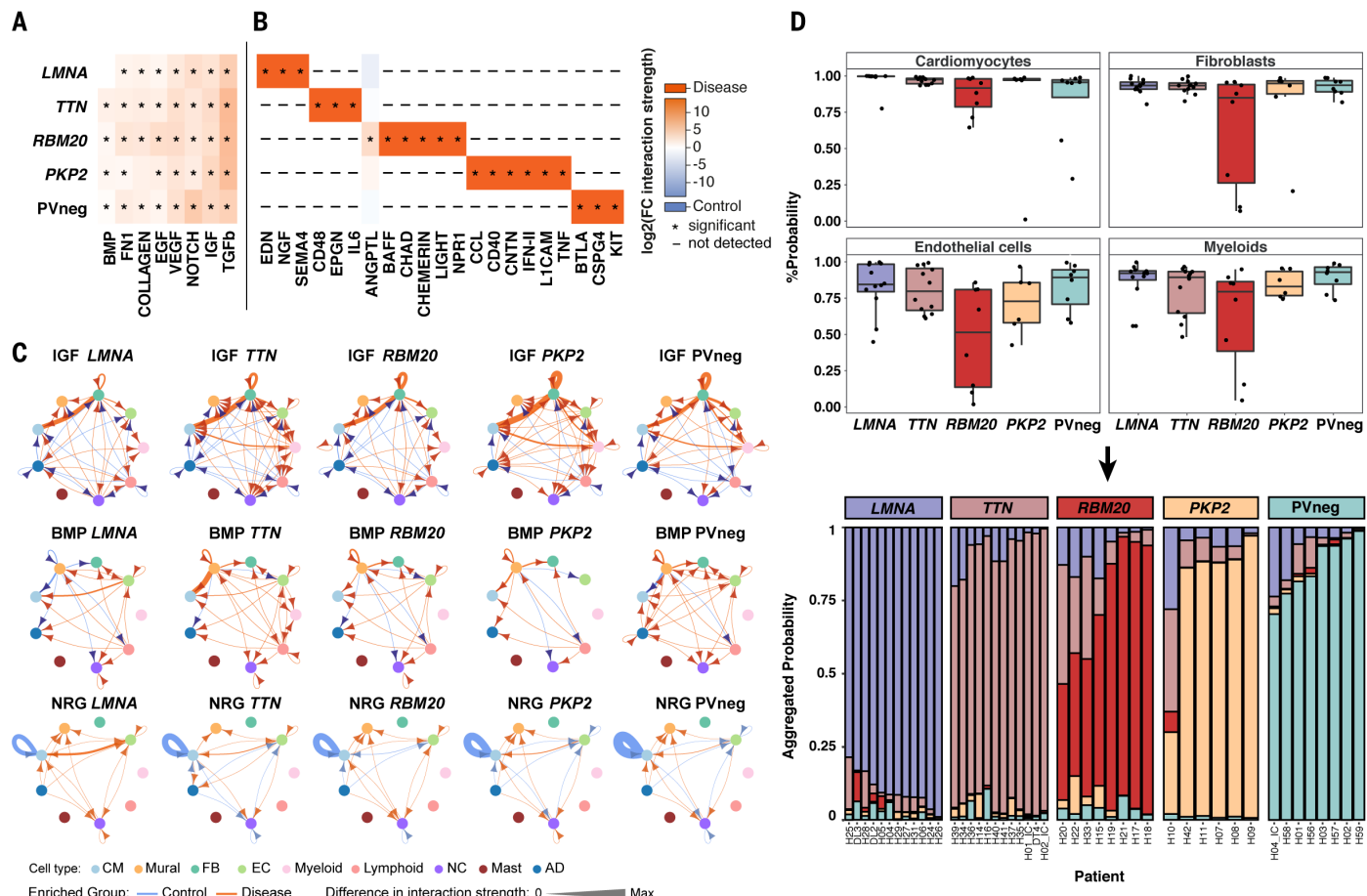


Fig. 6. Altered cell-cell interactions and recognition of genotype-specific transcriptional responses. Heatmaps depict shared (A) and unique (B) signaling pathways in LVs, with significantly different expression in genotypes compared with controls. Signaling pathways are defined in the CellChat database (75). Changes in interaction strength ($\log_2 FC$; table S68), scaled by color intensity (red, increased; blue, decreased). Asterisks denote statistical significance (adjusted P value ≤ 0.05); dashes indicate that expression was not detected in control or disease. (C) Circle plots of significant (adjusted P value ≤ 0.05) cell-cell communication depicting differentially regulated IGF, BMP, and NRG pathways.

pathways and interactions in disease LVs. The line thickness denotes interaction strength of signals from sending and receiving cells; color is scaled from zero to maximum in disease versus controls (orange, increased; blue, decreased). Arrows indicate directionality. (D) Top: Genotype prediction probability from GAT per cell type. Bottom: Stacked bar plots representing the likelihood (% aggregated probability) of individual patient genotypes by GAT prediction. Most established genotypes were predicted with high probability, with lower prediction probability only in H10 (*PKP2*), H20 (*RBM20*), H22 (*RBM20*), and H33 (*RBM20*).

in disease pathways (Fig. 6C). For example, IGF signaling (fig. S42), which is crucial in cell growth and CM hypertrophy, showed increased FB autocrine (highest in *PKP2*) and paracrine FB to CM signaling, paralleling findings in experimental models (76, 77). In addition, IGF signaling from myeloid cells to CMs only occurred in *TTN*, *PKP2*, and PVneg, an interaction that might promote muscle repair (78).

The source of BMP signaling changed in a genotype-specific manner (Fig. 6C and fig. S43). BMP signaling from MC to CM was increased in *TTN* LVs and RVs, but was down-regulated in PVneg and *LMNA* LVs and other RVs (figs. S41 and S43). BMP signaling in ECs originated solely from EC7, likely depending on *BMP6* up-regulation (Fig. 3, E and G). EDN signaling from EC7 to CM and MC was highly genotype selective, occurring in *LMNA* LV and *PKP2* RV (fig. S44).

NRG signaling (comprising *NRG1-3* and *ERBB* receptors) showed multifaceted changes. Disease LVs markedly attenuated autocrine NRG signaling in CMs, whereas EC and CM signaling was up-regulated (highest in *LMNA*) in all genotypes except *RBM20* (Fig. 6C and fig. S45). Additionally, NRG3-ERBB4 interactions identified in controls shifted in disease to NRG1-ERBB4 and NRG1-ERBB3 in a genotype-specific manner, consistent with changes in *NRG1/3* expression in EC7 (Fig. 3G and fig. S46) (79). This predicted NRG/ERBB shift may provide compensatory responses to adverse remodeling in cardiomyopathies (48).

Graph attention networks recognized genotype-specific expression patterns

We applied machine-learning approaches to snRNAseq data to further advance the recognition of cell- and genotype-specific transcriptional patterns. Cell-specific neighborhood graphs showed more connectivities among single-nuclei transcriptomes from PVneg hearts and hearts with PVs in the same gene compared with PVs from different genes (fig. S47). Subsequently, we generated a graph attention network (GAT) for multinomial classification of genotypes trained on four major informative LV cell types: CMs, FBs, ECs, and myeloids (fig. S47, A and B). The GAT predicted *LMNA*, *TTN*, *RBM20*, *PKP2*, and PVneg genotypes with high accuracy. Among LV samples, the genotype prediction accuracy differed by cell type: CMs, 0.93; FBs, 0.92; myeloids, 0.85; and ECs, 0.79 (Fig. 6D, fig. S48, and tables S69 to S70; corresponding RV data are shown in fig. S47C). Aggregation of genotype predictions obtained from these four LV cell types strengthened the correct prediction of genotypes, resulting in a high confidence model (Fig. 6D). Three (H10, H22, and H33) of the four lower prediction probabilities occurred in samples with both a primary and secondary PV, assigned as such by prior genotype and

clinical phenotype review (table S1). Moreover, because this machine-learning model independently confirmed a genotype- and cell-type-specific transcriptional signature, we concluded that these snRNAseq datasets accurately described the molecular responses to PVs and unexplained causes of DCM and ACM.

Discussion

Our analyses of snRNAseq of LV and RV samples illuminated the cell types and states, molecular signals, and predicted intercellular communications that characterized DCM and ACM. Compared with control hearts, we identified differences at multiple levels, including changes in the proportions of cell types and states, additional cell states, and differential gene expression, substantially expanding earlier insights achieved by bulk tissue analyses. Across all genotypes, diseased hearts demonstrated some common dissimilarities from control hearts, often with graded differences between LVs and RVs. Despite studying hearts from patients with advanced disease who received diverse therapies, congruent transcriptional signatures emerged for different PVs within the same gene and varied between genotypes.

The differences between genotype groups and controls reflected differences in mean expression and not differences in variance. This was true for each genotype group, including PVneg. Transcriptional signatures were complex, diversified both by the proportions of canonical and stressed cell states and by differentially expressed genes within the same states. Although interrogation of these datasets provides ongoing opportunities for discovery, our findings provided substantial evidence that genotype influenced pathological remodeling of the heart. These results upend a prevalent dogma that heart failure results from a common final pathway and can guide the future development of therapies with selective targets to enhance personalized medicine.

Despite anatomical and histopathological differences between DCM and ACM, we identified shared changes in the cellular composition of ventricular tissues, albeit with DCM LV features largely mirrored in ACM RVs. Cardiomyopathies were depleted in CMs, whereas EC and immune cell populations were increased. FBs did not expand, but increased states that augmented ECM gene expression and collagen deposition. Based on these changes and cytokine profiles (TGF β activation, increased IGF signaling, decreased *CCL2* expression; Fig. 2, H and I, and 6C), we predicted cell-cell interactions and key molecules that are appropriate for mechanistic studies to causally link differential expression with adverse cardiac remodeling.

Disease CMs exhibited loss of the canonical state vCM1.0 and the emergence of genotype-enriched cell states with DEGs. Many of these

responses are associated with stress-induced contractile, metabolic, and electrophysiologic properties that are prominent clinical manifestations of some genotypes. For example, attenuated expression of *SMYD1*, a critical organizer of sarcomere structure and epigenetic and metabolic remodeling, occurred only in CMs with PVs and was unaltered in PVneg samples. With its global impact on myocardial function, dysregulation of *SMYD1* might contribute to earlier presentation and poorer outcomes of cardiomyopathy patients with versus without PVs (80). *LMNA* CMs had the greatest expansion of vCM1.2, enriched for genes encoding Ca $^{2+}$ regulators and molecules with electrophysiologic functions, whereas *RBM20* and *LMNA* genotypes had the highest expression of *MYL4*, a sarcomere protein associated with atrial fibrillation. These data suggested molecular mechanisms whereby particular genotypes convey increased risks for arrhythmias and sudden cardiac death in patients.

Shifts in FB states explained the paradoxically increased fibrosis in cardiomyopathies, without expansion of overall FB populations. DCM LVs and ACM RVs showed increased proportions of vFB2, enriched for genes that modulate ECM composition, turnover, stiffness, and fibrotic scarring (81), and reciprocally decreased proportions of vFB3 that express transcripts suppressing fibrosis. Fibrogenic genes within vFB2 were highly expressed in *RBM20*, a genotype within our cohort with the poorest ventricular function and youngest age for heart failure diagnosis and cardiac transplantation. Strategies to manipulate proteins encoded by these genes may attenuate the prominent myocardial fibrosis that characterizes cardiomyopathies.

Unexpectedly, mural cells (PCs and SMCs) showed no increase compared with ECs across cardiomyopathies. DEG analysis suggested that these cells promoted vascular remodeling and dysfunction. PCs diminished *PDGFRB* expression and showed aberrant NOTCH signaling in vascular beds, whereas genotype-selective DEGs in SMCs up-regulated contractile genes, augmenting fiber formation. Together, these molecular signals may contribute to the microvascular dysfunction that occurs in cardiomyopathy patients (82) and adversely influences ventricular performance.

Among EC, EC7 demarcated the endocardium and had the most DEGs in disease compared with control. Little is known about this myocardial layer in heart failure pathogenesis. The endocardium forms through dynamic regulation of NOTCH, neuregulin (83), and BMP (84) signals. Pediatric heart diseases can exhibit pathological expansion of the endocardium (denoted endocardial fibroelastosis), which diminishes cardiac performance and is associated with progression to heart failure (84). Our data suggested similar dysregulation of

these molecular pathways in adult-onset cardiomyopathies with increased *BMP6* and *NRG1* in EC7 and decreased *INHBA* (53). These signals may cause pathological changes in endocardium in DCM and ACM hearts and contribute to myocardial dysfunction.

Diseased hearts had increased myeloid cells. Expansion of immune cell populations might arise from recruitment of circulating cells or proliferation of resident cells. In our samples, proliferating myeloid cells decreased, as was previously observed in other DCM studies (85). Myeloid recruitment through the CCR2/CCL2 axis, which is primarily mediated by vFB3, was decreased in all samples, with particularly dysregulated fibroblast-to-macrophage interactions in *TTN*. Although distinguishing between proliferation versus recruitment late in disease was problematic, previous studies indicated that peak cytokine expression precedes the emergence of heart failure (86, 87). Analyses of earlier time points during disease progression will be important to discern these key signals.

We used machine-learning strategies to confirm and expand the conclusion that genotype-specific signals meaningfully contribute to disease pathogenesis. Using GAT to classify patients' genotypes from each cell type, we found that CMs, FBs, ECs, and myeloid cells provided the highest and most discriminatory information. Harnessing LV and RV data from these cell types, we independently predicted the established genotype of each patient with high accuracy. Moreover, among the four samples with the lowest genotype-predictive probability, three samples carried two PVs, indicating that the model detected subtle transcriptional differences with additional influences.

Although expanding machine-learning models to much larger datasets will undoubtedly improve accuracy, these early analyses supported the conclusion that PVs in different genes evoked cell-type- and state-specific responses that altered intercellular communications and promoted distinct disease pathways. We recognize that pathways may converge, but even in advanced disease, our data indicate that genotypes promoted specific transcriptional signals that likely contributed to distinct as well as common manifestations of genetic cardiomyopathies.

Future studies are needed to comprehensively define the molecular pathophysiology of cardiomyopathies and heart failure, including assessments of age, sex, and ancestral influences; other DCM and ACM genotypes; additional cardiac regions; and longitudinal analyses to identify initiating and secondary processes. We also expect that the deployment of strategies that upsample conduction system and other rare cell types and the incorporation of techniques to characterize the epigenome, proteome, and spatial relationships between

cell types, states, and gene expression will also be highly informative. To promote these initiatives, we freely provide all datasets and an interactive platform (<https://cellxgene.cziscience.com/collections/e75342a8-0f3b-4ec5-8ee1-245a23e0f7cb>) with cell type and state annotations. We expect that these resources will advance mechanistic studies to improve treatment of cardiomyopathies and enable heart failure prevention strategies.

Methods summary

Detailed information on human subject studies, experimental methods, data access, codes, algorithms, and computational programs used in this manuscript is provided in the supplementary materials (88).

Human studies were performed using protocols that were reviewed and approved by the ethics boards of participating institutions. DCM and ACM ventricular samples were collected from genotyped patients undergoing mechanical support ($n = 15$) or heart transplantation ($n = 31$) and from deceased donors with nonfailing hearts as described previously. Nuclei from full-thickness LV and RV regions were isolated and processed for snRNAseq as described previously. Data were mapped to the human genome (GRCh38), processed to remove doublets and to identify nuclei that met high quality standards, and harmonized to remove batch effects. Manifolds were constructed using UMAPs for all and individual cell types.

Differential abundance analyses of cell types and states were performed using centered log ratio transformation including a linear model. Differential gene expression between disease and control tissues were deduced using a pseudobulk approach and EdgeR. Comparative analyses assessed cell type and cell state abundances and differential gene expression between disease samples and controls and between genotypes. Selected genes with differential expression were validated using single-molecule fluorescent *in situ* hybridization or quantitative immunohistochemistry.

We investigated cell-cell communication using CellChat. The expression of genes previously identified through GWAS of DCM was assessed in diseased and control tissues. We interrogated transcriptional datasets with machine-learning tools to generate cell type features that distinguished PVs within the same gene from PVs within different genes and used these data to generate a GAT. The accuracy for GAT analyses of randomly selected patient data to assign the correct, clinically assigned genotype was assessed.

REFERENCES AND NOTES

- E. M. McNally, L. Mestroni, Dilated cardiomyopathy: Genetic determinants and mechanisms. *Circ. Res.* **121**, 731–748 (2017). doi: [10.1161/CIRCRESAHA.116.309396](https://doi.org/10.1161/CIRCRESAHA.116.309396); pmid: [28912180](https://pubmed.ncbi.nlm.nih.gov/28912180/)
- K. M. Austin et al., Molecular mechanisms of arrhythmogenic cardiomyopathy. *Nat. Rev. Cardiol.* **16**, 519–537 (2019). doi: [10.1038/s41569-019-0200-7](https://doi.org/10.1038/s41569-019-0200-7); pmid: [31028357](https://pubmed.ncbi.nlm.nih.gov/31028357/)
- A. L. Bui, T. B. Horwitz, G. C. Fonarow, Epidemiology and risk profile of heart failure. *Nat. Rev. Cardiol.* **8**, 30–41 (2011). doi: [10.1038/nrcardio.2010.165](https://doi.org/10.1038/nrcardio.2010.165); pmid: [21060326](https://pubmed.ncbi.nlm.nih.gov/21060326/)
- M. Litvánková et al., Cells of the adult human heart. *Nature* **588**, 466–472 (2020). doi: [10.1038/s41586-020-2797-4](https://doi.org/10.1038/s41586-020-2797-4); pmid: [32971526](https://pubmed.ncbi.nlm.nih.gov/32971526/)
- J. S. Warren et al., Histone methyltransferase Smyd1 regulates mitochondrial energetics in the heart. *Proc. Natl. Acad. Sci. U.S.A.* **115**, E7871–E7880 (2018). doi: [10.1073/pnas.1800680115](https://doi.org/10.1073/pnas.1800680115); pmid: [30061404](https://pubmed.ncbi.nlm.nih.gov/30061404/)
- S. Franklin et al., The chromatin-binding protein Smyd1 restricts adult mammalian heart growth. *Am. J. Physiol. Heart Circ. Physiol.* **311**, H1234–H1247 (2016). doi: [10.1152/ajpheart.00235.2016](https://doi.org/10.1152/ajpheart.00235.2016); pmid: [27663768](https://pubmed.ncbi.nlm.nih.gov/27663768/)
- F. Steinberg, Beta₁-adrenergic receptor regulation revisited. *Circ. Res.* **123**, 1199–1201 (2018). doi: [10.1161/CIRCRESAHA.118.313884](https://doi.org/10.1161/CIRCRESAHA.118.313884); pmid: [30571467](https://pubmed.ncbi.nlm.nih.gov/30571467/)
- M. R. Bristol, Mechanism of action of beta-blocking agents in heart failure. *Am. J. Cardiol.* **80** (11A), 26L–40L (1997). doi: [10.1016/S0002-9149\(97\)00846-1](https://doi.org/10.1016/S0002-9149(97)00846-1); pmid: [9412540](https://pubmed.ncbi.nlm.nih.gov/9412540/)
- Y. Hasumi et al., Folliculin (Flcn) inactivation leads to murine cardiac hypertrophy through mTORC1 deregulation. *Hum. Mol. Genet.* **23**, 5706–5719 (2014). doi: [10.1093/hmg/ddu286](https://doi.org/10.1093/hmg/ddu286); pmid: [24908670](https://pubmed.ncbi.nlm.nih.gov/24908670/)
- H. Hasumi et al., Folliculin-interacting proteins Fnip1 and Fnip2 play critical roles in kidney tumor suppression in cooperation with Flcn. *Proc. Natl. Acad. Sci. U.S.A.* **112**, E1624–E1631 (2015). doi: [10.1073/pnas.1419502112](https://doi.org/10.1073/pnas.1419502112); pmid: [25775561](https://pubmed.ncbi.nlm.nih.gov/25775561/)
- K. Shen et al., Cryo-EM structure of the human FLCN-FNIP2-Rag-Ragulator complex. *Cell* **179**, 1319–1329.e8 (2019). doi: [10.1016/j.cell.2019.10.036](https://doi.org/10.1016/j.cell.2019.10.036); pmid: [31704029](https://pubmed.ncbi.nlm.nih.gov/31704029/)
- M. Mejias et al., CPEB4 increases expression of PFKFB3 to induce glycolysis and activate mouse and human hepatic stellate cells, promoting liver fibrosis. *Gastroenterology* **159**, 273–288 (2020). doi: [10.1053/j.gastro.2020.03.008](https://doi.org/10.1053/j.gastro.2020.03.008); pmid: [32169429](https://pubmed.ncbi.nlm.nih.gov/32169429/)
- R. Ajima et al., Deficiency of Myo18B in mice results in embryonic lethality with cardiac myofibrillar aberrations. *Genes Cells* **13**, 987–999 (2008). doi: [10.1111/j.1365-2443.2008.01226.x](https://doi.org/10.1111/j.1365-2443.2008.01226.x); pmid: [18761673](https://pubmed.ncbi.nlm.nih.gov/18761673/)
- M. Hueso et al., Silencing of CD40 in vivo reduces progression of experimental atherosclerosis through an NF-κB/miR-125b axis and reveals new potential mediators in the pathogenesis of atherosclerosis. *Atherosclerosis* **255**, 80–89 (2016). doi: [10.1016/j.atherosclerosis.2016.11.002](https://doi.org/10.1016/j.atherosclerosis.2016.11.002); pmid: [27835742](https://pubmed.ncbi.nlm.nih.gov/27835742/)
- S.-Y. Kim, S. Yasuda, H. Tanaka, K. Yamagata, H. Kim, Non-clustered protocadherin. *Cell Adh. Migr.* **5**, 97–105 (2011). doi: [10.4161/cam.5.12.4374](https://doi.org/10.4161/cam.5.12.4374); pmid: [21173574](https://pubmed.ncbi.nlm.nih.gov/21173574/)
- Y. Li et al., The N-cadherin interactome in primary cardiomyocytes as defined using quantitative proximity proteomics. *J. Cell Sci.* **132**, jcs.221606 (2019). doi: [10.1242/jcs.221606](https://doi.org/10.1242/jcs.221606); pmid: [30630894](https://pubmed.ncbi.nlm.nih.gov/30630894/)
- Y. Wang et al., PCDH7 interacts with GluN1 and regulates dendritic spine morphology and synaptic function. *Sci. Rep.* **10**, 10951 (2020). doi: [10.1038/s41598-020-67831-8](https://doi.org/10.1038/s41598-020-67831-8); pmid: [32616769](https://pubmed.ncbi.nlm.nih.gov/32616769/)
- P. D. Swaminathan, A. Purohit, T. J. Hund, M. E. Anderson, Calmodulin-dependent protein kinase II: Linking heart failure and arrhythmias. *Circ. Res.* **110**, 1661–1677 (2012). doi: [10.1161/CIRCRESAHA.111.243956](https://doi.org/10.1161/CIRCRESAHA.111.243956); pmid: [22679140](https://pubmed.ncbi.nlm.nih.gov/22679140/)
- L. A. Swayne et al., Novel variant in the ANK2 membrane-binding domain is associated with ankyrin-B syndrome and structural heart disease in a first nations population with a high rate of long QT syndrome. *Circ. Cardiovasc. Genet.* **10**, e001537 (2017). doi: [10.1161/CIRCGENETICS.116.001537](https://doi.org/10.1161/CIRCGENETICS.116.001537); pmid: [28196901](https://pubmed.ncbi.nlm.nih.gov/28196901/)
- H. D. Devalla et al., TECLRL, a new life-threatening inherited arrhythmia gene associated with overlapping clinical features of both LQTS and CPVT. *EMBO Mol. Med.* **8**, 1390–1408 (2016). doi: [10.15252/emmm.201505719](https://doi.org/10.15252/emmm.201505719); pmid: [27861123](https://pubmed.ncbi.nlm.nih.gov/27861123/)
- V. Gauvin et al., Alk3/Bmprla receptor is required for development of the atrioventricular canal into valves and annulus fibrosus. *Circ. Res.* **97**, 219–226 (2005). doi: [10.1161/01.RES.0000177862.85474.63](https://doi.org/10.1161/01.RES.0000177862.85474.63); pmid: [16037571](https://pubmed.ncbi.nlm.nih.gov/16037571/)
- N. W. Morrell et al., Targeting BMP signalling in cardiovascular disease and anaemia. *Nat. Rev. Cardiol.* **13**, 106–120 (2016). doi: [10.1038/nrcardio.2015.156](https://doi.org/10.1038/nrcardio.2015.156); pmid: [26461965](https://pubmed.ncbi.nlm.nih.gov/26461965/)
- J. Filmus, M. Capurro, The role of glycans in Hedgehog signaling. *Matrix Biol.* **35**, 248–252 (2014). doi: [10.1016/j.matbio.2013.12.007](https://doi.org/10.1016/j.matbio.2013.12.007); pmid: [24412155](https://pubmed.ncbi.nlm.nih.gov/24412155/)

24. M. L. Schmitz, M. S. Shaban, B. V. Albert, A. Gökçen, M. Kracht, The crosstalk of endoplasmic reticulum (ER) stress pathways with NF- κ B: Complex mechanisms relevant for cancer, inflammation and infection. *Biomedicines* **6**, 58 (2018). doi: [10.3390/biomedicines6020058](https://doi.org/10.3390/biomedicines6020058); pmid: [29772680](#)
25. M. Wilhelm et al., Sh3rf2/POSHER protein promotes cell survival by ring-mediated proteasomal degradation of the c-Jun N-terminal kinase scaffold POSH (Plenty of SH3s) protein. *J. Biol. Chem.* **287**, 2247–2256 (2012). doi: [10.1074/jbc.M111.269431](https://doi.org/10.1074/jbc.M111.269431); pmid: [22128169](#)
26. R. Eckenstaler, J. Sandor, M. Gekle, R. A. Benndorf, Angiotensin II receptor type 1 - An update on structure, expression and pathology. *Biochem. Pharmacol.* **192**, 114673 (2021). doi: [10.1016/j.bcp.2021.114673](https://doi.org/10.1016/j.bcp.2021.114673); pmid: [3425409](#)
27. H. Itabashi et al., Angiotensin II and epidermal growth factor receptor cross-talk mediated by a disintegrin and metalloprotease accelerates tumor cell proliferation of hepatocellular carcinoma cell lines. *Hepatol. Res.* **38**, 601–613 (2008). doi: [10.1111/j.1872-034X.2007.00304.x](https://doi.org/10.1111/j.1872-034X.2007.00304.x); pmid: [18452483](#)
28. C. F. Baicu et al., Effects of the absence of procollagen C-endopeptidase enhancer-2 on myocardial collagen accumulation in chronic pressure overload. *Am. J. Physiol. Heart Circ. Physiol.* **303**, H234–H240 (2012). doi: [10.1152/ajpheart.00227.2012](https://doi.org/10.1152/ajpheart.00227.2012); pmid: [22610170](#)
29. K. J. Travaglini et al., A molecular cell atlas of the human lung from single-cell RNA sequencing. *Nature* **587**, 619–625 (2020). doi: [10.1038/s41586-020-2922-4](https://doi.org/10.1038/s41586-020-2922-4); pmid: [33208946](#)
30. S. Schafer et al., IL-11 is a crucial determinant of cardiovascular fibrosis. *Nature* **552**, 110–115 (2017). doi: [10.1038/nature24676](https://doi.org/10.1038/nature24676); pmid: [29160304](#)
31. S. Nandadasa, C. M. Nelson, S. S. Apte, ADAMTS9-mediated extracellular matrix dynamics regulates umbilical cord vascular smooth muscle differentiation and rotation. *Cell Rep.* **11**, 1519–1528 (2015). doi: [10.1016/j.celrep.2015.05.005](https://doi.org/10.1016/j.celrep.2015.05.005); pmid: [26027930](#)
32. B.-H. Koo et al., ADAMTS9 is a cell-autonomously acting, anti-angiogenic metalloprotease expressed by microvascular endothelial cells. *Am. J. Pathol.* **176**, 1494–1504 (2010). doi: [10.2353/ajpath.2010.090655](https://doi.org/10.2353/ajpath.2010.090655); pmid: [2093484](#)
33. T. Nadeem, W. Bogue, B. Bigit, H. Cuervo, Deficiency of Notch signaling in pericytes results in arteriovenous malformations. *JCI Insight* **5**, e125940 (2020). doi: [10.1172/jci.insight.125940](https://doi.org/10.1172/jci.insight.125940); pmid: [33148887](#)
34. P. U. Magnusson et al., Platelet-derived growth factor receptor-beta constitutive activity promotes angiogenesis in vivo and in vitro. *Arterioscler. Thromb. Vasc. Biol.* **27**, 2142–2149 (2007). doi: [10.1161/01.ATV.0000282198.60701.94](https://doi.org/10.1161/01.ATV.0000282198.60701.94); pmid: [17656670](#)
35. S. Jin et al., Notch signaling regulates platelet-derived growth factor receptor- β expression in vascular smooth muscle cells. *Circ. Res.* **102**, 1483–1491 (2008). doi: [10.1161/CIRCRESAHA.107.167965](https://doi.org/10.1161/CIRCRESAHA.107.167965); pmid: [18483410](#)
36. V. Domenga et al., Notch3 is required for arterial identity and maturation of vascular smooth muscle cells. *Genes Dev.* **18**, 2730–2735 (2004). doi: [10.1101/gad.308904](https://doi.org/10.1101/gad.308904); pmid: [15545631](#)
37. A. H. Campos, W. Wang, M. J. Pollman, G. H. Gibbons, Determinants of Notch-3 receptor expression and signaling in vascular smooth muscle cells: Implications in cell-cycle regulation. *Circ. Res.* **91**, 999–1006 (2002). doi: [10.1161/01.RES.0000044944.9998.25](https://doi.org/10.1161/01.RES.0000044944.9998.25); pmid: [12456485](#)
38. I. Marek et al., Alpha8 integrin (Itga8) signaling attenuates chronic renal interstitial fibrosis by reducing fibroblast activation, not by interfering with regulation of cell turnover. *PLOS ONE* **11**, e0150471 (2016). doi: [10.1371/journal.pone.0150471](https://doi.org/10.1371/journal.pone.0150471); pmid: [26938996](#)
39. C. F. Hung, C. L. Wilson, Y.-H. Chow, L. M. Schnapp, Role of integrin alpha8 in murine model of lung fibrosis. *PLOS ONE* **13**, e0197937 (2018). doi: [10.1371/journal.pone.0197937](https://doi.org/10.1371/journal.pone.0197937); pmid: [29813125](#)
40. J. J. Connelly et al., Epigenetic regulation of COL15A1 in smooth muscle cell replicative aging and atherosclerosis. *Hum. Mol. Genet.* **22**, 5107–5120 (2013). doi: [10.1093/hmg/ddt365](https://doi.org/10.1093/hmg/ddt365); pmid: [23912340](#)
41. L. Gong et al., SLIT3 deficiency attenuates pressure overload-induced cardiac fibrosis and remodeling. *JCI Insight* **5**, e136852 (2020). doi: [10.1172/jci.insight.136852](https://doi.org/10.1172/jci.insight.136852); pmid: [32644051](#)
42. R. Sewduth, M. M. Santoro, "Decoding" angiogenesis: New facets controlling endothelial cell behavior. *Front. Physiol.* **7**, 306 (2016). doi: [10.3389/fphys.2016.00306](https://doi.org/10.3389/fphys.2016.00306); pmid: [27493632](#)
43. S. L. House et al., Endothelial fibroblast growth factor receptor signaling is required for vascular remodeling following cardiac ischemia-reperfusion injury. *Am. J. Physiol. Heart Circ. Physiol.* **310**, H559–H571 (2016). doi: [10.1152/ajpheart.00758.2015](https://doi.org/10.1152/ajpheart.00758.2015); pmid: [26747503](#)
44. X.-B. Cui, S.-Y. Chen, Response gene to complement 32 in vascular diseases. *Front. Cardiovasc. Med.* **5**, 128 (2018). doi: [10.3389/fcvm.2018.00128](https://doi.org/10.3389/fcvm.2018.00128); pmid: [30280101](#)
45. Y. Xiao et al., Hippo signaling plays an essential role in cell state transitions during cardiac fibroblast development. *Dev. Cell* **45**, 153–169.e6 (2018). doi: [10.1016/j.devcel.2018.03.019](https://doi.org/10.1016/j.devcel.2018.03.019); pmid: [2968192](#)
46. J. Tang et al., Genetic fate mapping defines the vascular potential of endocardial cells in the adult heart. *Circ. Res.* **122**, 984–993 (2018). doi: [10.1161/CIRCRESAHA.117.312354](https://doi.org/10.1161/CIRCRESAHA.117.312354); pmid: [29374073](#)
47. R. A. Norris et al., Periostin regulates atrioventricular valve maturation. *Dev. Biol.* **316**, 200–213 (2008). doi: [10.1016/j.ydbio.2008.01.003](https://doi.org/10.1016/j.ydbio.2008.01.003); pmid: [18313657](#)
48. G. W. De Keulenaer et al., Mechanisms of the multitasking endothelial protein NRG-1 as a compensatory factor during chronic heart failure. *Circ. Heart Fail.* **12**, e006288 (2019). doi: [10.1161/CIRCHEARTFAILURE.119.006288](https://doi.org/10.1161/CIRCHEARTFAILURE.119.006288); pmid: [31607147](#)
49. X.-S. Zhao, W. Pan, R. Bekerjian, R. V. Shohet, Endogenous endothelin-1 is required for cardiomyocyte survival in vivo. *Circulation* **114**, 830–837 (2006). doi: [10.1161/CIRCULATIONAHA.105.577288](https://doi.org/10.1161/CIRCULATIONAHA.105.577288); pmid: [16908774](#)
50. C. K. Hathaway et al., Endothelin-1 critically influences cardiac function via superoxide-MMP9 cascade. *Proc. Natl. Acad. Sci. U.S.A.* **112**, 5141–5146 (2015). doi: [10.1073/pnas.1504557112](https://doi.org/10.1073/pnas.1504557112); pmid: [25848038](#)
51. R. Y. Kim, E. J. Robertson, M. J. Solloway, Bmp6 and Bmp7 are required for cushion formation and septation in the developing mouse heart. *Dev. Biol.* **235**, 449–466 (2001). doi: [10.1006/dbio.2001.0284](https://doi.org/10.1006/dbio.2001.0284); pmid: [11437450](#)
52. Y. Fang et al., Tbx20 induction promotes zebrafish heart regeneration by inducing cardiomyocyte dedifferentiation and endocardial expansion. *Front. Cell Dev. Biol.* **8**, 738 (2020). doi: [10.3389/fcell.2020.00738](https://doi.org/10.3389/fcell.2020.00738); pmid: [32850848](#)
53. A. C. Y. Chang et al., Notch initiates the endothelial-to-mesenchymal transition in the atrioventricular canal through autocrine activation of soluble guanylyl cyclase. *Dev. Cell* **21**, 288–300 (2011). doi: [10.1016/j.devcel.2011.06.022](https://doi.org/10.1016/j.devcel.2011.06.022); pmid: [21839921](#)
54. A. Puig-Kröger et al., Folate receptor beta is expressed by tumor-associated macrophages and constitutes a marker for M2 anti-inflammatory/regulatory macrophages. *Cancer Res.* **69**, 9395–9403 (2009). doi: [10.1158/0008-5472.CAN-09-2050](https://doi.org/10.1158/0008-5472.CAN-09-2050); pmid: [19951991](#)
55. S. A. Dick et al., Self-renewing resident cardiac macrophages limit adverse remodeling following myocardial infarction. *Nat. Immunol.* **20**, 29–39 (2019). doi: [10.1038/s41590-018-0272-2](https://doi.org/10.1038/s41590-018-0272-2); pmid: [30538339](#)
56. M. Pérez-Hernández et al., Transcriptomic coupling of PKP2 with inflammatory and immune pathways endogenous to adult cardiac myocytes. *Front. Physiol.* **11**, 623190 (2021). doi: [10.3389/fphys.2020.623190](https://doi.org/10.3389/fphys.2020.623190); pmid: [33536940](#)
57. A. M. van der Leun, D. S. Thommen, T. N. Schumacher, CD8⁺ T cell states in human cancer: Insights from single-cell analysis. *Nat. Rev. Cancer* **20**, 218–232 (2020). doi: [10.1038/s41568-019-0235-4](https://doi.org/10.1038/s41568-019-0235-4); pmid: [32024970](#)
58. J. G. Barin, D. Číháková, Control of inflammatory heart disease by CD4+ T cells. *Ann. N. Y. Acad. Sci.* **1285**, 80–96 (2013). doi: [10.1111/nyas.12134](https://doi.org/10.1111/nyas.12134); pmid: [23692566](#)
59. D. Vdovenko, U. Eriksson, Regulatory role of CD4⁺ T cells in myocarditis. *J. Immunol. Res.* **2018**, 4396351 (2018). doi: [10.1155/2018/4396351](https://doi.org/10.1155/2018/4396351); pmid: [30035131](#)
60. C. Kim et al., LRRK2 mediates microglial neurotoxicity via NFATc2 in rodent models of synucleinopathies. *Sci. Transl. Med.* **12**, eaay0399 (2020). doi: [10.1126/scitranslmed.aay0399](https://doi.org/10.1126/scitranslmed.aay0399); pmid: [33055242](#)
61. N. B. Schwartz, M. S. Domowicz, Proteoglycans in brain development and pathogenesis. *FEBS Lett.* **592**, 3791–3805 (2018). doi: [10.1002/1873-3468.13026](https://doi.org/10.1002/1873-3468.13026); pmid: [29513405](#)
62. H. Zhu et al., The complement regulator Sust4 influences nervous-system function and neuronal morphology in mice. *iScience* **23**, 100957 (2020). doi: [10.1016/j.isci.2020.100957](https://doi.org/10.1016/j.isci.2020.100957); pmid: [32179479](#)
63. R. Méndez-Giráldez et al., GWAS of the electrocardiographic QT interval in Hispanics/Latinos generalizes previously identified loci and identifies population-specific signals. *Sci. Rep.* **7**, 17075 (2017). doi: [10.1038/s41598-017-17136-0](https://doi.org/10.1038/s41598-017-17136-0); pmid: [29213071](#)
64. A. H. Christensen et al., The two-pore domain potassium channel TWIK-1, has a role in the regulation of heart rate and atrial size. *J. Mol. Cell. Cardiol.* **97**, 24–35 (2016). doi: [10.1016/j.jmcc.2016.04.006](https://doi.org/10.1016/j.jmcc.2016.04.006); pmid: [27103460](#)
65. X. Xu et al., Methamphetamine exposure triggers apoptosis and autophagy in neuronal cells by activating the C/EBP β -related signaling pathway. *FASEB J.* **32**, 6737–6759 (2018). doi: [10.1096/fj.201701460RRR](https://doi.org/10.1096/fj.201701460RRR)
66. P. E. Schauwecker, Galanin receptor 1 deletion exacerbates hippocampal neuronal loss after systemic kainate administration in mice. *PLOS ONE* **5**, e15657 (2010). doi: [10.1371/journal.pone.0015657](https://doi.org/10.1371/journal.pone.0015657); pmid: [2179451](#)
67. V. Beaumont et al., Phosphodiesterase 10A inhibition improves cortico-basal ganglia function in huntington's disease models. *Neuron* **92**, 1220–1237 (2016). doi: [10.1016/j.neuron.2016.10.064](https://doi.org/10.1016/j.neuron.2016.10.064); pmid: [27916455](#)
68. Y. Mitome-Mishima et al., Differences in phosphodiesterase 3A and 3B expression after ischemic insult. *Neurosci. Res.* **75**, 340–348 (2013). doi: [10.1016/j.neures.2013.02.006](https://doi.org/10.1016/j.neures.2013.02.006); pmid: [23471014](#)
69. C. Chitraju, T. C. Walther, R. V. Farese Jr., The triglyceride synthesis enzymes DGAT1 and DGAT2 have distinct and overlapping functions in adipocytes. *J. Lipid Res.* **60**, 1112–1120 (2019). doi: [10.1194/jlr.M093112](https://doi.org/10.1194/jlr.M093112); pmid: [30936184](#)
70. M. Schweiger et al., G0/G1 switch gene-2 regulates human adipocyte lipolysis by affecting activity and localization of adipose triglyceride lipase. *J. Lipid Res.* **53**, 2307–2317 (2012). doi: [10.1194/jlr.M027409](https://doi.org/10.1194/jlr.M027409); pmid: [22891293](#)
71. M. A. Sanders, H. Zhang, L. Mladenovic, Y. Y. Tseng, J. G. Granneman, Molecular basis of ABHD5 lipolysis activation. *Sci. Rep.* **7**, 42589 (2017). doi: [10.1038/srep42589](https://doi.org/10.1038/srep42589); pmid: [28211464](#)
72. K. Onoue et al., Cardiomyocyte proliferative capacity is restricted in mice with *Lmna* mutation. *Front. Cardiovasc. Med.* **8**, 639148 (2021). doi: [10.3389/fcvm.2021.639148](https://doi.org/10.3389/fcvm.2021.639148); pmid: [34250035](#)
73. M. P. Morley et al., Cardioprotective effects of MTSS1 enhancer variants. *Circulation* **139**, 2073–2076 (2019). doi: [10.1161/CIRCULATIONAHA.118.037939](https://doi.org/10.1161/CIRCULATIONAHA.118.037939); pmid: [31070942](#)
74. H. V. Meyer et al., Genetic and functional insights into the fractal structure of the heart. *Nature* **584**, 589–594 (2020). doi: [10.1038/s41586-020-2635-8](https://doi.org/10.1038/s41586-020-2635-8); pmid: [32814899](#)
75. S. Jin et al., Inference and analysis of cell-cell communication using CellChat. *Nat. Commun.* **12**, 1088 (2021). doi: [10.1038/s41467-021-21246-9](https://doi.org/10.1038/s41467-021-21246-9); pmid: [33597522](#)
76. N. Takeda et al., Cardiac fibroblasts are essential for the adaptive response of the murine heart to pressure overload. *J. Clin. Invest.* **120**, 254–265 (2010). doi: [10.1172/JCI40295](https://doi.org/10.1172/JCI40295); pmid: [20038803](#)
77. T. Horio et al., Production and autocrine/paracrine effects of endogenous insulin-like growth factor-1 in rat cardiac fibroblasts. *Regul. Pept.* **124**, 65–72 (2005). doi: [10.1016/j.regpep.2004.06.029](https://doi.org/10.1016/j.regpep.2004.06.029); pmid: [15544842](#)
78. J. Tonkin et al., Monocyte/macrophage-derived IGF-1 orchestrates murine skeletal muscle regeneration and modulates autocrine polarization. *Mol. Ther.* **23**, 1189–1200 (2015). doi: [10.1038/mtn.2015.66](https://doi.org/10.1038/mtn.2015.66); pmid: [25896247](#)
79. O. Odiete, M. F. Hill, D. B. Sawyer, Neuregulin in cardiovascular development and disease. *Circ. Res.* **111**, 1376–1385 (2012). doi: [10.1161/CIRCRESAHA.112.267286](https://doi.org/10.1161/CIRCRESAHA.112.267286); pmid: [23104879](#)
80. L. Escobar-Lopez et al., Association of genetic variants with outcomes in patients with nonischemic dilated cardiomyopathy. *J. Am. Coll. Cardiol.* **78**, 1682–1699 (2021). doi: [10.1016/j.jacc.2021.08.039](https://doi.org/10.1016/j.jacc.2021.08.039); pmid: [34674813](#)
81. P. Kong, P. Christia, N. G. Frangogiannis, The pathogenesis of cardiac fibrosis. *Cell. Mol. Life Sci.* **71**, 549–574 (2014). doi: [10.1007/s00018-013-1349-6](https://doi.org/10.1007/s00018-013-1349-6); pmid: [23649149](#)
82. A. Gulati et al., Microvascular dysfunction in dilated cardiomyopathy: A quantitative stress perfusion cardiovascular magnetic resonance study. *JACC Cardiovasc. Imaging* **12**, 1699–1708 (2019). doi: [10.1016/j.jcmg.2018.10.032](https://doi.org/10.1016/j.jcmg.2018.10.032); pmid: [30660522](#)
83. G. del Monte-Nieto et al., Control of cardiac jelly dynamics by NOTCH1 and NRG1 defines the building plan for trabeculation. *Nature* **557**, 439–445 (2018). doi: [10.1038/s41586-018-0110-6](https://doi.org/10.1038/s41586-018-0110-6); pmid: [29743679](#)
84. X. Xu et al., Endocardial fibroelastosis is caused by aberrant endothelial to mesenchymal transition. *Circ. Res.* **116**, 857–866 (2015). doi: [10.1161/CIRCRESAHA.116.305629](https://doi.org/10.1161/CIRCRESAHA.116.305629); pmid: [25587097](#)
85. R. O. Ramirez Flores et al., Consensus transcriptional landscape of human end-stage heart failure. *J. Am. Heart Assoc.* **10**, e019667 (2021). doi: [10.1161/JAHF.120.019667](https://doi.org/10.1161/JAHF.120.019667); pmid: [33787284](#)
86. X. Liao et al., Distinct roles of resident and nonresident macrophages in nonischemic cardiomyopathy. *Proc. Natl. Acad. Sci. U.S.A.* **115**, E4661–E4669 (2018). doi: [10.1073/pnas.1720065115](https://doi.org/10.1073/pnas.1720065115); pmid: [29712858](#)

87. O. Dewald *et al.*, CCL2/Monocyte Chemoattractant Protein-1 regulates inflammatory responses critical to healing myocardial infarcts. *Circ. Res.* **96**, 881–889 (2005). doi: [10.1161/01.RES.0000163017.13772.3a](https://doi.org/10.1161/01.RES.0000163017.13772.3a); pmid: [15774854](https://pubmed.ncbi.nlm.nih.gov/15774854/)
88. The supplemental materials are available online.
89. E. Lindberg *et al.*, Code for: "Pathogenic variants damage cell composition and single cell transcription in cardiomyopathies"heiniglab/DCM_heart_cell_atlas: v1.0 release," Zenodo, Version 1 (2022); .doi: [10.5281/zenodo.6720185](https://doi.org/10.5281/zenodo.6720185)

ACKNOWLEDGMENTS

The authors extend their heartfelt gratitude to the patients and relatives who provided cardiac tissues for research and to the biobanks who supported these efforts: Biobank of the Heart and Diabetes Center NRW, University Hospital of the Ruhr-University Bochum, the HELP Program (Mazankowski Alberta Heart Institute) and HOPE program (University of Alberta Hospital), the Cardiovascular Research Centre Biobank at the Royal Brompton and Harefield hospitals and NHS Blood and Transplant, and the Brigham and Women's Cardiovascular Tissue Bank. We also thank H.-P. Rahn of the Flow Cytometry Technology Platform, the Systems Biology Imaging Platform (both MDC), T. Borodina of the BIH/MDC Genomics Technology Platform, and S. Schmidt (MDC) for technical help in single-nuclei isolation and library preparation; the Facility for Imaging by Light Microscopy and S. Rothery (Imperial College London) and the LMS/NIHR Imperial Biomedical Research Centre Flow Cytometry Facility for support; L. Lawrence from the Research Histology Facility at Imperial College, the Biopolymers Laboratory, P. Montero Llopis of the Microscopy Resources on the North Quad (MicRoN) core (Harvard Medical School), and G. Plummer at the Faculty of Medicine & Dentistry Cell Imaging Core (University of Alberta) for technical support; D. Keimüller for advice on machine learning; and S. Bartlett (Brigham and Women's Hospital and Harvard Medical School) for administrative assistance. **Funding:** This project has been made possible in part by the Chan Zuckerberg Foundation (2019-202666) to N.H., M.H., M.N., C.E.S., J.G.S., and S.A.T.; the Leducq Foundation (16CVD03) to N.H., C.E.S., and J.G.S.; the British Heart Foundation and Deutsches Zentrum für Herz-Kreislauf-Forschung (BHF/DZHK: SP/19/1/34461) to N.H., M.N., and S.A.T.; the Medical Faculty of the Ruhr-University, FoRUM (F842R-2015) to H.Mi., A.G. & J.G.; the Deutsche Forschungsgemeinschaft to H.Mi. (1164.6-1, and 1146.2-2), to N.H. (SFB-1470 – B03) and to D.R. (Research Fellowship); the Wellcome Trust (107469/Z/15/Z; 200990/A/16/Z) to J.S.W. and to S.A.T. (206194, 108413/A/15/D), the Medical Research Council (UK), the National Institute for Health Research (NIHR) Royal Brompton Cardiovascular Biomedical Research Unit and NIHR Imperial College Biomedical Research Centre to J.S.W. and P.J.B.; the National Institutes of Health (HL080494 and HL084553)

to C.E.S. and J.G.S and to Y.K. (KL2-TR002542); the Engineering Research Centers Program of the National Science Foundation (NSF Cooperative Agreement EEC-1647837) to C.E.S. and J.G.S.; the John S. LaDue Fellowship of Harvard Medical School to Y.K. and K.B.; the Wellcome Trust Clinical PhD Fellowship to J.C.; the Overseas Research Fellowship of the Takeda Science Foundation to K.K., the Stanley Sarnoff Foundation Fellowship to E.R.N.; Boehringer Ingelheim Fonds to V.S.; the Brigham and Women's Hospital Khoury Innovation Award to Y.K.; the Ludwig Institute for Cancer Research grant, National Cancer Institute grant (U54-CA225088) and CCSF Supplemental Award to C.Y.; the British Heart Foundation (RE/18/4/34215) to J.S.W.; the ERC-advanced grant under the European Union Horizon 2020 Research and Innovation Program (AdG788970) to N.H.: the University of Alberta Hospital Foundation (UHF), the Canadian Institute of Health Research (CIHR), the Heart and Stroke Foundation (HSF), and the Canada Research Chair in Heart Failure to G.Y.O.; the Choudhrie Family Fund and Howard Hughes Medical Institute to C.E.S. **Author contributions:** Conceptualization: M.H., N.H., H.Ma., H.Mi., M.N., G.Y.O., C.E.S., J.G.S.; Methodology: M.H., N.H., E.L.L., H.Ma., H.Mi., M.N., G.Y.O., D.R., C.E.S., J.G.S.; Patient recruitment, clinical data analyses, tissue procurement, patient genotyping, and biobanking: P.J.R.B., R.A.C., A.G., L.M., H.Mi., Y.K., B.M., M.N., G.Y.O., C.E.S., P.I.T., A.v.d.B., J.S.W.; Sample processing (tissue preparation, nuclei isolation, library prep, sequencing): R.J.B., D.R.D., L.E.F., J.M.G., A.Gh., E.L.L., Y.A.L., L.M., D.R., G.P., V.S., J.G.S., A.V., H.W., H.Z.; Data analysis: C.M., D.R., C.E.S., J.G.S., F.B.: E.A., N.H., M.K., E.L.L., H.Ma., EC: A.M.A.M., M.N., C.L.W., Myeloid: N.H., M.K., E.L.L., H.Ma., Lymphoid: J.C., K.K., R.L., S.A.T., MC: N.H. M.K., E.L.L., H.Ma., J.R.-O., NC: E.R.N., D.R., C.E.S., J.G.S., Adipocytes: M.L., M.N., Compositional: M.H., F.S., F.J.T., J.G.S., Data interpretation: All histology, immunostaining, single-molecule in situ hybridization, microscopy: K.B., S.N.B., E.L.L., A.M.A.M., E.R.N., D.R., V.S., A.V., H.W., A.W., H.Z.; GWAS: P.J.R.B., M.H.; CellChat: M.L., A.M.A.M., M.N.; GAT: E.L.L., C.L., N.S.; Online data hosting: M.H.; Writing: E.A., N.H., E.L.L., M.L., A.M.A.M., H.Ma., E.R.N., D.R., J.R.-O., N.S., C.E.S., J.G.S.; Review and editing: E.A., P.J.R.B., N.H., E.L.L., H.Ma., H.Mi., M.N., G.Y.O., D.R., C.E.S., J.G.S.; Supervision: P.J.R.B., M.H., N.H., H.Ma., H.Mi., M.N., G.Y.O., C.E.S., J.G.S., S.A.T., F.T.; Funding: P.J.R.B., M.H., N.H., H.Mi., M.N., G.Y.O., C.E.S., J.G.S., S.A.T., J.S.W. **Competing interests:** The following authors report competing interests. Consultancy fees: J.S.W. (MyoKardia Inc, and Foresite Labs); C.E.S. and J.G.S. (Maze, BridgeBio, Bristol Myers Squibb); S.A.T. (Genentech and Roche). Scientific advisory boards: S.A.T. (Biogen, GlaxoSmithKline, Qiagen and Foresite Labs). Board of directors: C.E.S. (Burroughs Wellcome Fund U.S. and Merck). Co-founder and equity holder: S.A.T. (Transition Bio). J.S.W. acknowledges research support from MyoKardia, Bristol Myers Squibb, and Pfizer (formerly Array BioPharma). These companies were not involved in any aspect of

the study's experimental design, execution, and analyses or in the preparation of the manuscript. D.R., E.L.L., H.M., A.M.A.M., A.V., N.S., A.G., E.R.N., M.L., K.K., J.R.-O., V.S., D.M.D., G.P., H.Z., A.W., C.L., Y.K., E.A., J.M.G., S.N.G., K.B., R.J.B., R.A.C., C.C., J.C., L.E.F., H.F., A.G., M.K., R.L., L.M., B.M., S.S., F.S., C.Y., C.S., P.I.T., F.J.T., A.v.d.B., H.W., C.L.W., P.J.R.B., Y.A.L., H.M., M.N., G.Y.O., M.H., and N.H. declare no competing interests. **Data and materials availability:** All sequence data generated and analyzed in this study have been deposited as BAM files at the European Genome-phenome Archive (EGA), which is hosted by the EBI and the CRG, under accession number EGAS00001006374 (<https://ega-archive.org/studies/EGAS00001006374>). Further information about EGA can be found on <https://ega-archive.org>, "The European Genome-phenome Archive in 2021" (<https://academic.oup.com/nar/advance-article/doi/10.1093/nar/gkab1059/6430505>). Processed data can be analyzed using the Celxgene tool website: <https://celxgene.cziscience.com/collections/e75342a8-0f3b-4ec5-8ee1-245a23e07cb/private> and are available in h5ad format to download. Metadata sheets and patient information are available in tables S1 and S2. All code used to generate the figures in this publication are available on GitHub (https://github.com/heiniglab/DCM_heart_cell_atlas). Code used to reproduce the presented analyses is indexed on Zenodo (89). All scripts run on jupyter notebooks are available as ".ipynb" files, and scripts executed in command line are available as .txts or .sh files. R scripts are available as ".R". Anaconda environments are available as yml files containing information on package versions. **License information:** Copyright © 2022 the authors, some rights reserved; exclusive licensee American Association for the Advancement of Science. No claim to original US government works. <https://www.science.org/about/science-licenses-journal-article-reuse>. This research was funded in whole or in part by the Howard Hughes Medical Institute, a cOAdition S organization. The author will make the Author Accepted Manuscript (AAM) version available under a CC BY public copyright license.

SUPPLEMENTARY MATERIALS

science.org/doi/10.1126/science.abo1984

Materials and Methods

Figs. S1 to S53

Tables S1 to S71

References (90–129)

MDAR Reproducibility Checklist

[View/request a protocol for this paper from Bio-protocol](https://www.bio-protocol.org).

Submitted 20 January 2022; accepted 1 July 2022

10.1126/science.abo1984